

The following article has been submitted to The Journal of Chemical Physics. ©2021 Yasutaka Yamaguchi. This article is distributed under a Creative Commons Attribution (CC BY) License.

Curvature dependence of the interfacial tensions around nanoscale cylinder: Young's equation still holds

Keitaro Watanabe,^{1, a)} Hiroki Kusudo,^{1, b)} Carlos Bistafa,^{1, c)} Takeshi Omori,^{2, d)} and Yasutaka Yamaguchi^{1, 3, e)}

¹⁾*Department of Mechanical Engineering, Osaka University, 2-1 Yamadaoka, Suita 565-0871, Japan*

²⁾*Department of Mechanical Engineering, Osaka City University, 3-3-138 Sugimoto, Sumiyoshi, Osaka 558-8585, Japan*

³⁾*Water Frontier Research Center (WaTUS), Research Institute for Science & Technology, Tokyo University of Science, 1-3 Kagurazaka, Shinjuku-ku, Tokyo, 162-8601, Japan*

(Dated: 29 November 2021)

By extending the theoretical framework derived in our previous study [Y. Imaizumi et al., J. Chem. Phys. 153, 034701 (2020)], we successfully calculated the solid-liquid (SL) and solid-vapor (SV) interfacial tensions of a simple Lennard-Jones fluid around solid cylinders with nanometer-scale diameters from single equilibrium molecular dynamics (MD) systems, in which a solid cylinder was vertically immersed into a liquid pool. The SL and SV interfacial tensions $\gamma_{\text{SL}} - \gamma_{\text{S0}}$ and $\gamma_{\text{SV}} - \gamma_{\text{S0}}$ relative to that for bare solid surface γ_{S0} , respectively were obtained by simple force balance relations on fluid-containing control volumes set around the bottom and top of the solid cylinder, which are subject to the fluid stress and the force from the solid. The theoretical contact angle calculated by Young's equation using these interfacial tensions agreed well with the apparent contact angle estimated by the analytical solution fitted to the meniscus shape, showing that Young's equation holds even for the menisci around solids with nanoscale curvature. We have also found that the curvature effect on the contact angle was surprisingly small while it was indeed large on the local forces exerted on the solid cylinder near the contact line. In addition, the present results showed that the curvature dependence of the SL and SV interfacial free energies, which are the interfacial tensions, is different from that of the corresponding interfacial potential energies.

^{a)}present affiliation: Department of Management of Industry and Technology, Osaka University

^{b)}Electronic mail: hiroki@nnfm.mech.eng.osaka-u.ac.jp

^{c)}Electronic mail: bistafa@nnfm.mech.eng.osaka-u.ac.jp

^{d)}Electronic mail: omori@osaka-cu.ac.jp

^{e)}Electronic mail: yamaguchi@mech.eng.osaka-u.ac.jp

I. INTRODUCTION

As we see cap-shaped liquid droplets on solid surfaces almost everyday, wetting behavior is one of the most common physical phenomena in human life, and is also a topic of interest in various scientific and engineering fields.^{1–5} By introducing the concept of interfacial tensions and contact angle θ , wetting is usually described by Young’s equation⁶ given by

$$\gamma_{\text{SL}} - \gamma_{\text{SV}} + \gamma_{\text{LV}} \cos \theta = 0, \quad (1)$$

where γ_{SL} , γ_{SV} and γ_{LV} denote solid-liquid (SL), solid-vapor (SV) and liquid-vapor (LV) interfacial tensions, respectively. Young’s equation (1) was first proposed based on the wall-tangential force balance of interfacial tensions exerted on the contact line (CL) in 1805 – before the establishment of thermodynamics⁷ –, now it is often explained from a thermodynamic point of view instead of the mechanical force balance.¹ Practically, the contact angle is used as a common measure of wettability. Various models have been proposed to capture the details of the CL, such as introducing the concept of precursor film^{1,8} or the microscopic contact angle,⁹ or considering the effects of line tension due to the contact-line curvature in Eq. (1).^{10,11} However, it is difficult to experimentally validate these models mainly because measuring the interfacial tensions γ_{SL} and γ_{SV} , which include the solid phase, is not trivial.^{12,13}

Wetting plays a key role especially in the nanoscale with a large surface to volume ratio, and from a microscopic point of view, Kirkwood and Buff¹⁴ first provided the theoretical framework of surface tension based on the statistical mechanics. Recent development of molecular simulation methods including molecular dynamics (MD) and Monte Carlo (MC) advanced the microscopic understanding of the interfaces, and the calculation of the surface tension based on Bakker’s equation,^{2,3,15} which describes the relation between the stress integral around the liquid-vapor or liquid-gas interface and the surface tension, is used as a standard approach.¹⁶ In addition, MD or MC studies about microscopic wetting have been conducted, ranging from simply evaluating the apparent contact angle, *e.g.*, from the average droplet shape, to quantitatively extract the SL and SV interfacial tensions through a mechanical manner and/or a thermodynamic manner.^{17–44} For the mechanical approach – called the mechanical route –, Bakker’s equation was extended to describe the connection between the stress integral through the SL or SV interface and the corresponding interfacial tension (See Appendix A).^{23–29} On the other hand for the latter approach – called the

thermodynamic route –, the SL and SV interfacial tensions were interpreted as the interfacial free energy per interfacial area. For instance, by the thermodynamic integration method, the SL interfacial energy was evaluated as the free energy difference from a reference system, in which the SL interface was substituted by bare solid and liquid surfaces quasi-statically under constant number of particles N , temperature T and pressure p (NpT -ensemble) or volume V (NVT -ensemble) condition.^{27–36} These studies indicated that the apparent contact angle of the meniscus or droplet obtained in the simulations agreed well with the one predicted by Young’s equation (1) in case the solid surfaces are flat and smooth so that the CL pinning may not be induced.^{28,29}

Considering the potential applications of nano-wetting, *e.g.*, a flow in a confined space such as a nanofoam⁴⁵ or a carbon nanotube,⁴⁶ the solid surfaces can have a nanoscale radius of curvature, and the interfacial tensions should depend on the curvature. Regarding the water wetting on carbon nanotubes as a solid with a nanoscale curvature, unique wetting behavior⁴⁷ and a strong diameter dependence of the capillary force were experimentally reported.⁴⁸ For the liquid-vapor interface, Tolman⁴⁹ first formulated the size effect of droplet surface tension with a lengthscale called the “Tolman length,”^{50–52} and MD or MC simulations have been carried out as well.^{38,53–57} Indeed, the LV interfacial tension can be extracted using a strict definition of the interface position, *e.g.*, based on the force and momentum balances,⁵³ and the difference between the pressures inside and outside the droplet based on the Young-Laplace equation. On the other hand, the calculation of the SL and SV interfacial tension on a curved solid surface is not trivial.^{55,58} For instance, via thermodynamic routes, if we suppose calculation systems for the thermodynamic integration to calculate the SL interfacial tension on a cylindrical solid surface with a nanoscale radius, then the three interface areas, *i.e.*, the radii of the target solid-fluid interface, the reference bare solid and bare liquid interfaces should be all different, and this difference would become critical for the evaluation of the desired interfacial tension when the cylinder radius is comparable to the radius differences. Another possibility is via mechanical routes, and it is technically possible to calculate the stress distribution in the cylindrical or spherical coordinates, although the calculation cost significantly increases to obtain the distribution, and indeed, precise calculation in these coordinate systems is not implemented into the MD packages such as LAMMPS⁵⁹ or GROMACS⁶⁰, and the implementation into in-house codes is also rather complicated.^{53,61}

Going back to the relation between the SL or SV interfacial tension and the fluid stress in the interface via the mechanical routes, what we need is not the stress distribution but the stress integral. Considering this feature, in our previous study,²⁶ we provided a theoretical framework to extract the SL and SV interfacial tensions from a single MD simulation by using the local forces and the local interaction potential exerted on a quasi-two-dimensional (2D) flat and smooth solid plate immersed into a liquid pool of a simple liquid, called the Wilhelmy plate, and verified through the comparison between the MD results and the interfacial works of adhesion obtained by the thermodynamic integration (TI). This modified Wilhelmy method is advantageous because it does not require computationally demanding calculations such as the local stress distributions and the thermodynamic integration which needs averaging at each discrete states along the integration path.

In this study, we extracted the SL and SV interfacial tensions of a simple Lennard-Jones fluid around solid cylinders with nanometer-scale radii by applying the modified Wilhelmy equations derived in our previous study²⁶ to investigate the curvature effect on the SL and SV interfacial tensions. From the results, we also examined whether Young's equation holds even for menisci around solids with nanoscale curvature. Finally, we discuss the difference in the curvature dependence between the SL and SV interfacial tensions (free energy) and the SL and SV interaction potential energies (part of internal energy).

II. METHOD

A. MD Simulation

In this study, we employed equilibrium MD simulation systems of a quasi-axisymmetric meniscus on a hollow cylinder dipped into a liquid pool of a simple fluid as shown in Fig. 1. Except the boundary condition in the lateral directions, the basic setup is similar to our previous study of quasi-2D meniscus formed on a hollow rectangular solid plate.²⁶ Generic particles interacting through a LJ potential were adopted as the fluid particles. The 12-6 LJ potential given by

$$\Phi^{\text{LJ}}(r_{ij}) = 4\epsilon \left[\left(\frac{\sigma}{r_{ij}} \right)^{12} - \left(\frac{\sigma}{r_{ij}} \right)^6 + c_2^{\text{LJ}} \left(\frac{r_{ij}}{r_c} \right)^2 + c_0^{\text{LJ}} \right], \quad (2)$$

was used for the interaction between fluid particles, where r_{ij} is the distance between the particles i at position \mathbf{r}_i and j at \mathbf{r}_j , while ϵ and σ denote the LJ energy and length

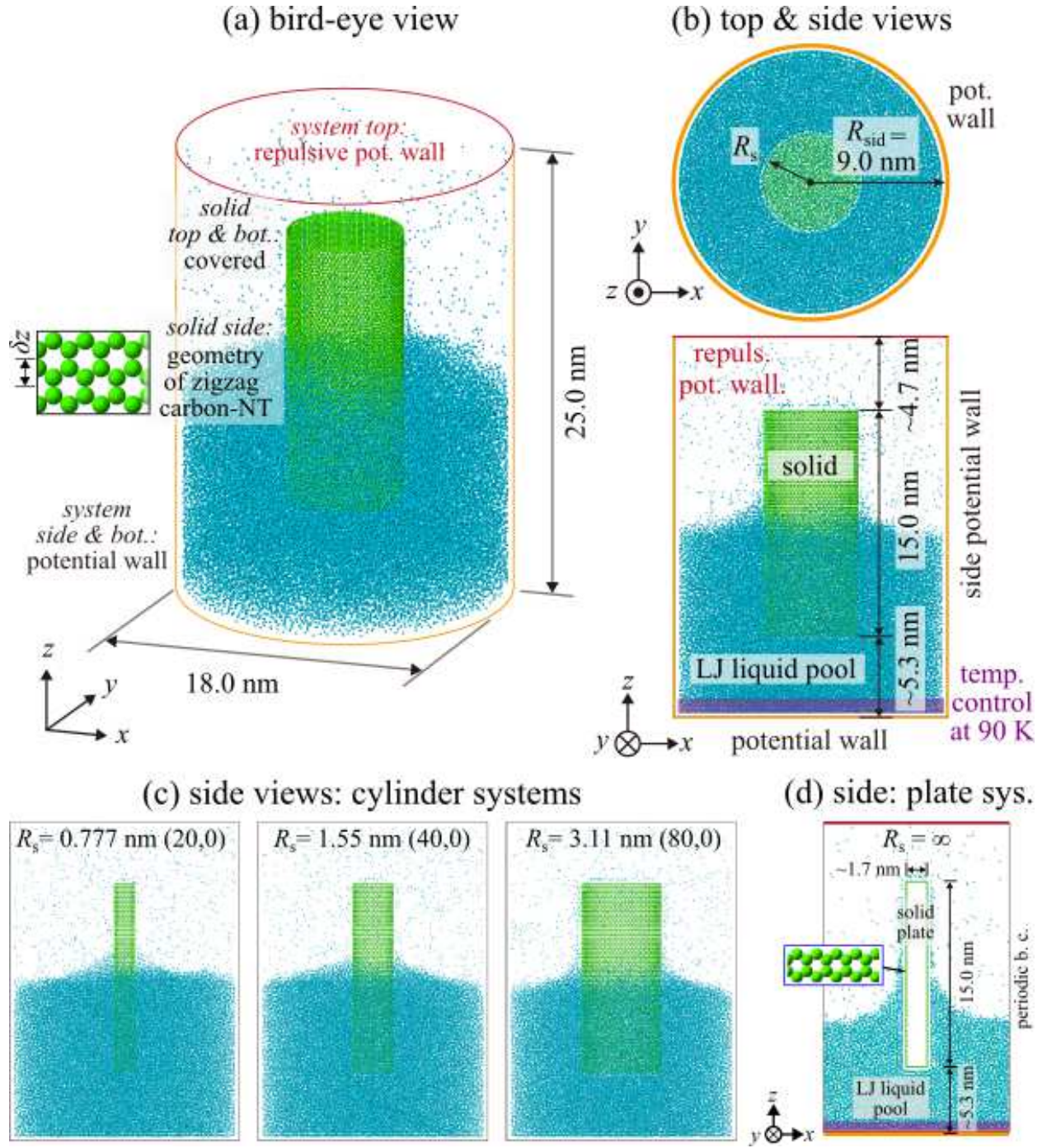


FIG. 1. (a) A bird-eye view and (b) top and (c) side views of equilibrium molecular dynamics (MD) simulation systems of hollow solid cylinders dipped into a liquid pool of a simple Lennard-Jones (LJ) fluid. (d) Side view of the system with a hollow solid plate [see Ref. 26 for details].

parameters, respectively. This LJ interaction was truncated at a cut-off distance of $r_c = 3.5\sigma$ and quadratic functions were added so that the potential and interaction force smoothly vanished at r_c . The constant values of c_2^{LJ} and c_0^{LJ} were given in our previous study.²⁵ Hereafter, fluid and solid particles are denoted by ‘f’ and ‘s’, respectively and corresponding combinations are indicated by subscripts.

Three solid cylinders in contact with the fluid were prepared by using the geometrical configuration of carbon nanotubes (CNTs) with their chiral indices of (20,0), (40,0) and (80,0), where the solid particles were fixed on the coordinate with the positions of hexagonal periodic structure with an inter-particle distance r_{ss} of 0.141 nm. Note that the solid surface is considered to be smooth with r_{ss} much smaller than σ_{ff} and σ_{sf} , and pinning is not induced on this surface. The corresponding radii R_s of the cylinder are 0.777, 1.55 and 3.11 nm, respectively. The central axis of the cylinders is set on the z -axis, *i.e.*, the zigzag edge of the honeycomb structure was set parallel to the xy -plane. The top and bottom parts of the cylinders are covered by locating additional solid particles as the lid to prevent fluid particles from entering into the cylinder. Note that the structure of these lids does not have direct effect on the simulation results as indicated in our previous study.²⁶

The solid-fluid (SF) interaction, which denotes SL or SV interaction, was also expressed by the LJ potential in Eq. (2), where the length parameter σ_{sf} was given by the Lorentz mixing rule, while the energy parameter ϵ_{sf} was changed in a parametric manner by multiplying a SF interaction coefficient η to the base value $\epsilon_{\text{sf}}^0 = \sqrt{\epsilon_{\text{ff}}\epsilon_{\text{ss}}}$ as

$$\epsilon_{\text{sf}} = \eta \epsilon_{\text{sf}}^0. \quad (3)$$

This parameter η expressed the wettability, *i.e.*, η and the contact angle of a hemi-cylindrically shaped equilibrium droplet on a homogeneous flat solid surface had a one-to-one correspondence^{25,28,29}, and we set the parameter η between 0.03 and 0.15 so that the corresponding cosine of the contact angle $\cos\theta$ is from -0.9 to 0.9 . The definition of the contact angle is described later in Sec. III. Note that due to the fact that the solid-solid inter-particle distance r_{ss} shown in Table I were relatively small compared to the LJ length parameters σ_{ff} and σ_{fs} , the surface is considered to be very smooth, and the wall-tangential force from the solid on the fluid, which induces pinning of the CL, is negligible.^{28,29}

We set a horizontal potential wall on the bottom (floor) of the calculation cell fixed at $z = z_{\text{flr}}$ about 5.3 nm below the bottom of the solid plate, which interacted only with the

fluid particles with a one-dimensional potential field $\Phi_{\text{flr}}^{\text{1D}}$ as the function of the distance from the wall given by

$$\Phi_{\text{flr}}^{\text{1D}}(z'_i) = 4\pi\rho_n\epsilon_{\text{sf}}^{\text{flr}}\sigma_{\text{sf}}^2 \left[\frac{1}{5} \left(\frac{\sigma_{\text{sf}}}{z'_i} \right)^{10} - \frac{1}{2} \left(\frac{\sigma_{\text{sf}}}{z'_i} \right)^4 + c_2^{\text{flr}} \left(\frac{z'_i}{z_c^{\text{flr}}} \right)^2 + c_1^{\text{flr}} \left(\frac{z'_i}{z_c^{\text{flr}}} \right) + c_0^{\text{flr}} \right], \quad (4)$$

$$z'_i \equiv z_i - z_{\text{flr}}. \quad (5)$$

where z_i is the z -position of fluid particle i , and $\epsilon_{\text{sf}}^{\text{flr}}$ is set at $0.09\epsilon_{\text{sf}}^0$. This potential wall mimicked a mean potential field created by a single layer of solid particles with a uniform area number density ρ_n . Similar to Eq. (2), this potential field in Eq. (4) was truncated at a cut-off distance of $z_c^{\text{flr}} = 3.5\sigma_{\text{sf}}$ and a quadratic function was added so that the potential and interaction force smoothly vanished at z_c^{flr} . As shown in Fig. 1, fluid particles were rather strongly attracted on this plane because this roughly corresponded to a solid wall showing complete wetting. With this setup, the liquid pool was stably kept even when the liquid pressure is low with a highly wettable solid plate, and sufficient liquid bulk region was formed between this wall and the bottom of the cylinder. Furthermore, we set another horizontal potential wall on the top (ceiling) of the calculation cell fixed at $z = z_{\text{ceil}}$ about 4.7 nm above the top of the solid plate exerting a repulsive potential field $\Phi_{\text{ceil}}^{\text{1D}}$ on the fluid particles given by

$$\Phi_{\text{ceil}}^{\text{1D}}(z''_i) = 4\pi\rho_n\epsilon_{\text{sf}}^{\text{ceil}}\sigma_{\text{sf}}^2 \left[\frac{1}{5} \left(\frac{\sigma_{\text{sf}}}{z''_i} \right)^{10} + c_2^{\text{ceil}} \left(\frac{z''_i}{z_c^{\text{ceil}}} \right)^2 + c_1^{\text{ceil}} \left(\frac{z''_i}{z_c^{\text{ceil}}} \right) + c_0^{\text{ceil}} \right], \quad (6)$$

$$z''_i \equiv z_{\text{ceil}} - z_i, \quad (7)$$

where $\epsilon_{\text{sf}}^{\text{ceil}}$ is equal to $\epsilon_{\text{sf}}^{\text{flr}}$ while a cut-off distance of $z_c^{\text{ceil}} = \sigma_{\text{sf}}$ is set to express a repulsive potential wall.

In addition to these bottom and top potential walls, we also set another cylindrical side potential wall with its axis on the z -axis and with a radius R_{sid} , which exerts a one-dimensional potential field on the fluid particles $\Phi_{\text{sid}}^{\text{1D}}(r_i^{xy})$ as the function of the horizontal distance from the wall given by

$$\Phi_{\text{sid}}^{\text{1D}}(r_i^{xy}) = 4\pi\rho_n\epsilon_{\text{sf}}^{\text{sid}}\sigma_{\text{sf}}^2 \left[\frac{1}{5} \left(\frac{\sigma_{\text{sf}}}{r_i^{xy}} \right)^{10} - \frac{1}{2} \left(\frac{\sigma_{\text{sf}}}{r_i^{xy}} \right)^4 + c_2^{\text{flr}} \left(\frac{r_i^{xy}}{r_c^{\text{sid}}} \right)^2 + c_1^{\text{flr}} \left(\frac{r_i^{xy}}{r_c^{\text{sid}}} \right) + c_0^{\text{sid}} \right], \quad (8)$$

$$r_i^{xy} \equiv R_{\text{sid}} - \sqrt{x_i^2 + y_i^2}, \quad (9)$$

where r_i^{xy} is the lateral distance of fluid particle i from the side potential wall. Note that this side wall was adopted to achieve a quasi-axisymmetric 2D-meniscus instead of applying the

periodic boundary condition in the horizontal x - and y -directions as in our previous study with a solid plate. The parameter $\epsilon_{\text{sf}}^{\text{sid}}$ was set at $0.0975\epsilon_{\text{sf}}^0$ so that the resulting contact angle at the side wall may be roughly 90 degrees.

The temperature of the system was maintained at a constant temperature of T_c at 90 K, which is above the triple point temperature⁶², by applying velocity rescaling to the fluid particles within 0.8 nm from the floor wall regarding the velocity components in the x - and y -directions. Note that this region was sufficiently away from the bottom of the solid plate and no direct thermostating was imposed on the region near the solid plate, so that this temperature control had no effects on the present results.

With this setting, an axisymmetric quasi-2D LJ liquid with a meniscus-shaped LV interface and the CL parallel to the xy -plane was formed as an equilibrium state as exemplified in Fig. 1, where a liquid bulk with an isotropic density distribution existed above the bottom wall by choosing a proper number of fluid particles N_f as shown in Fig. 2. We checked that the temperature was constant in the whole system after the equilibration run described below. The velocity Verlet method was applied for the integration of the Newtonian equation of motion with a time increment of 5 fs for all systems. The simulation parameters are summarized in Table I with the corresponding non-dimensional ones, which are normalized by the corresponding standard values based on ϵ_{ff} , σ_{ff} and m_f .

The physical properties of each equilibrium system with various η values were calculated as the time average of 20 ns which followed an equilibration run of more than 10 ns.

III. RESULTS AND DISCUSSION

A. Apparent contact angle

Similar to our previous study,²⁶ we calculated the distribution of force exerted from the fluid on the solid particles by dividing the system into equal-sized bins in the z -direction, where a bin height of $\delta z = 0.2115$ nm was used, considering the periodicity of the CNT structure. We defined the average force density $d\xi_z/dz$ as the time-averaged total downward (in $-z$ -direction) force from the fluid on the solid particles in each bin divided by the solid bin area $2\pi R_s \delta z$. Except at the top and bottom of the solid plate, $d\xi_z/dz$ corresponds to the downward force per surface area. We also calculated the average SF potential energy per

TABLE I. Simulation parameters and their corresponding non-dimensional values.

| property | value | unit | non-dim. value |
|--------------------------------------|--------------------------------------|------|----------------|
| σ_{ff} | 0.340 | nm | 1 |
| σ_{sf} | 0.357 | nm | 1.05 |
| r_{ss} | 0.141 | nm | 0.415 |
| ϵ_{ff} | 1.67×10^{-21} | J | 1 |
| ϵ_{sf}^0 | 1.96×10^{-21} | J | 1.18 |
| $\epsilon_{\text{sf}}^{\text{flr}}$ | 0.176×10^{-21} | J | 0.106 |
| $\epsilon_{\text{sf}}^{\text{ceil}}$ | 0.176×10^{-21} | J | 0.106 |
| $\epsilon_{\text{sf}}^{\text{sid}}$ | 0.192×10^{-21} | J | 0.115 |
| ϵ_{sf} | $\eta \times \epsilon_{\text{sf}}^0$ | | |
| η | 0.03 – 0.15 | - | - |
| m_{f} | 6.64×10^{-26} | kg | 1 |
| R_{s} | 0.777 – 3.11 | nm | 2.29 – 9.15 |
| T_{c} | 90 | K | 0.703 |
| N_{f} | 53778 - 60834 | - | - |

area u_{sf} , which was obtained by the same procedure but substituting the downward force by the SF potential energy.

Figure 2 shows a half side-snapshot and the distribution of time-averaged fluid density ρ around the solid cylinder for the system with solid-fluid interaction parameter $\eta = 0.15$. The time-averaged distributions of the downward force acting on the solid plate $d\xi_z/dz$ and the SF potential energy u_{sf} are also displayed in the right panel. We briefly summarize two essential features below, which are qualitatively the same as in our previous study.²⁶

1) Multi-layered adsorption layers were formed around the solid cylinder and the bottom and side potential walls, and liquid bulk with a homogeneous density is observed away from the cylinder, potential walls and the LV interface. 2) The total downward force as the integral of $d\xi_z/dz$ can be clearly separated into three local parts, *i.e.*, ξ_z^{top} around the top, ξ_z^{cl} around the contact line, and ξ_z^{bot} around the bottom. As indicated in Fig. 2 (c), ξ_z^{top} and ξ_z^{cl} are positive, *i.e.*, downward forces, and ξ_z^{bot} is negative, *i.e.*, an upward force. Note that the distributions of $d\xi_z/dz$ and u_{sf} around the top and bottom had less physical meaning

(a) side snapshot (b) fluid dens. dist. (c) down. force and sf-pot. ene. dist.

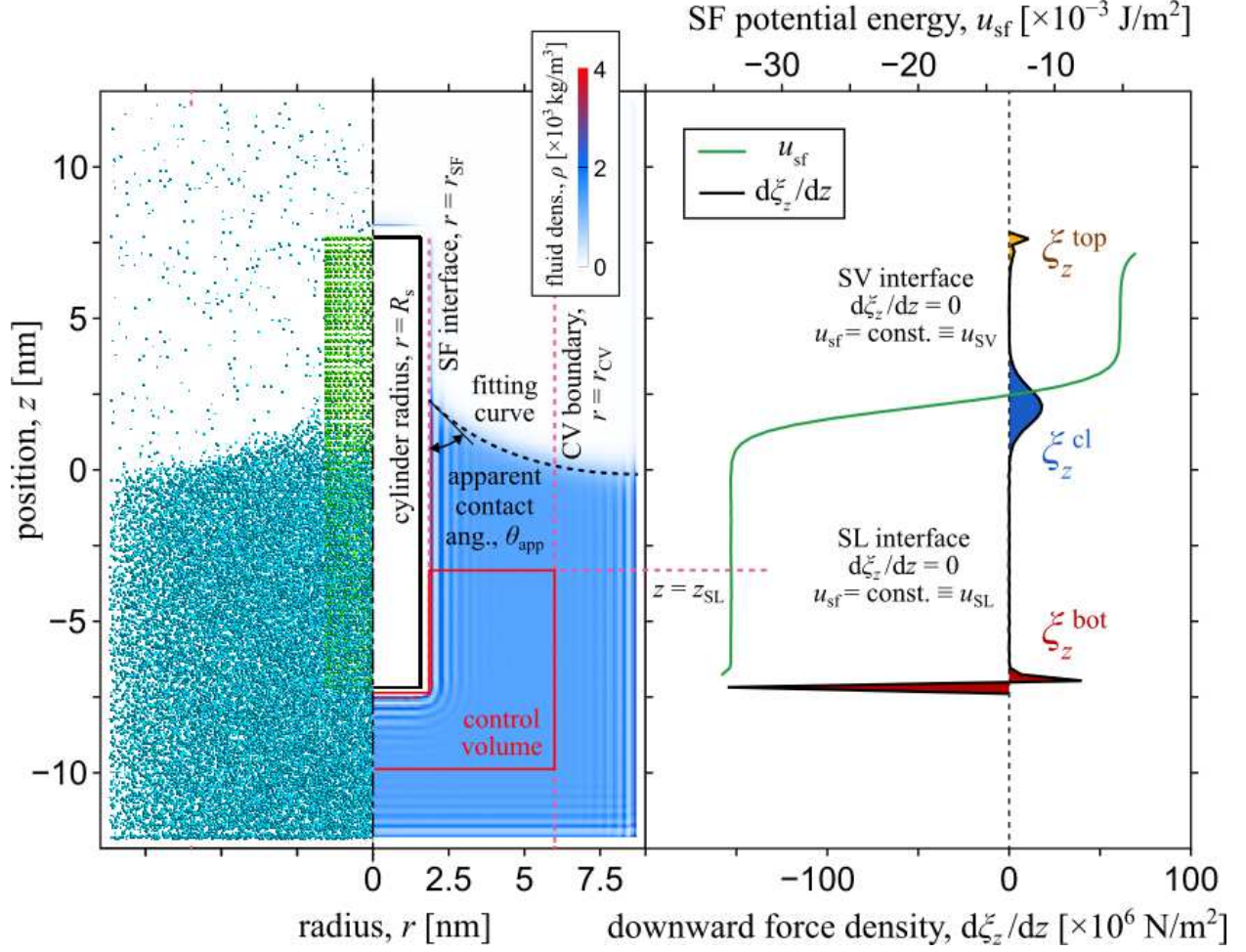


FIG. 2. (a) Half side snapshot, (b) distribution of the time-averaged fluid density, and (c) distributions of the time-averaged downward force density acting on the solid plate and solid-fluid (SF) potential energy density per solid surface area for the system with the solid radius $R_s = 1.55$ nm and a SF interaction parameter $\eta = 0.15$.

because they included the top and bottom solid lids in the bin, and these parts for u_{sf} are not displayed in the figure. However, the local integral of $d\xi_z^z/dz$ indeed gave the physical information about the force around the top and bottom parts. Also, note that ξ_z has the same dimension as the surface tension of force per length.

As exemplified in the density distribution in Fig. 2 (b), we evaluated the contact angles for the plate and cylinder systems with different solid-fluid interaction parameter to examine the curvature effects. For the plate system, we followed the same procedure used to determine

the apparent contact angle as our previous study:²⁶ the LV interface was defined as the least-squares fitting circle on the density contour of $\rho = 400 \text{ kg/m}^3$ at the LV interface at height $z(x)$ excluding the region in the adsorption layers near the solid,^{25,26,28,29} considering that with a constant liquid-vapor interfacial tension γ_{LV} the static force balance is written as

$$\frac{d}{dx} [\sin \psi(x)] = \frac{p_V^{\text{blk}} - p_L^{\text{blk}}}{\gamma_{LV}}, \quad \tan \psi(x) = \frac{dz(x)}{dx}, \quad (10)$$

where $\psi(x)$, p_V^{blk} and p_L^{blk} denote the angle from the x -direction and bulk pressure values in the vapor and liquid bulk, respectively. The solution of Eq. (10) results in a constant curvature with constant γ_{LV} , p_V^{blk} and p_L^{blk} . Then, by setting the solid-fluid (SF) interface position $r = r_{\text{SF}}$ as the limit that the fluid could reach, which can be easily estimated from the density distribution, we defined the apparent contact angle θ_{app} by the angle between the extrapolation of the cylindrical LV-interface and SF-interface plane at $r = r_{\text{SF}}$. This definition provided a mechanical description consistent with Young's equation.²⁸

Similarly, the contact angles on the cylinders were evaluated using the analytical formula of the macroscopic meniscus shape. For an axisymmetric equilibrium meniscus around a z -centered cylinder with neglecting gravity, it follows for the meniscus height $z(r)$ given as a unique function of the radial position $r \equiv \sqrt{x^2 + y^2}$ that

$$\frac{1}{r} \frac{d}{dr} [r \sin \psi(r)] = \frac{p_V^{\text{blk}} - p_L^{\text{blk}}}{\gamma_{LV}}, \quad \tan \psi(r) = \frac{dz(r)}{dr}, \quad (11)$$

where $\psi(r)$ denote the angle from the r -direction. We evaluated the three constant values in this differential equation (11) from MD simulations: γ_{LV} was obtained from a MD system with planer LV interfaces by a standard mechanical process,²⁷ whereas p_V^{blk} and p_L^{blk} were evaluated as the force per area on the top and bottom potential walls of the present cylinder system, respectively, both excluding the region near the side wall. Thus, by fitting the density contour of $\rho = 400 \text{ kg/m}^3$ at the LV interface excluding the region in the adsorption layers formed near the solid surface and also excluding that near the side potential wall, a numerical solution of the 2nd-order ordinary differential equation (11) can be obtained for each system with different cylinder radius R_s and solid-fluid interaction parameter η . As shown by the dotted black line in Fig. 2, the meniscus shape is well reproduced in this system. We determined the contact angle as the angle between the extrapolated solution of the meniscus shape and the SF-interface position in the rz -plane including the liquid side. We assume a concave control volume (CV) shown in red color in Fig. 2 (b) around the

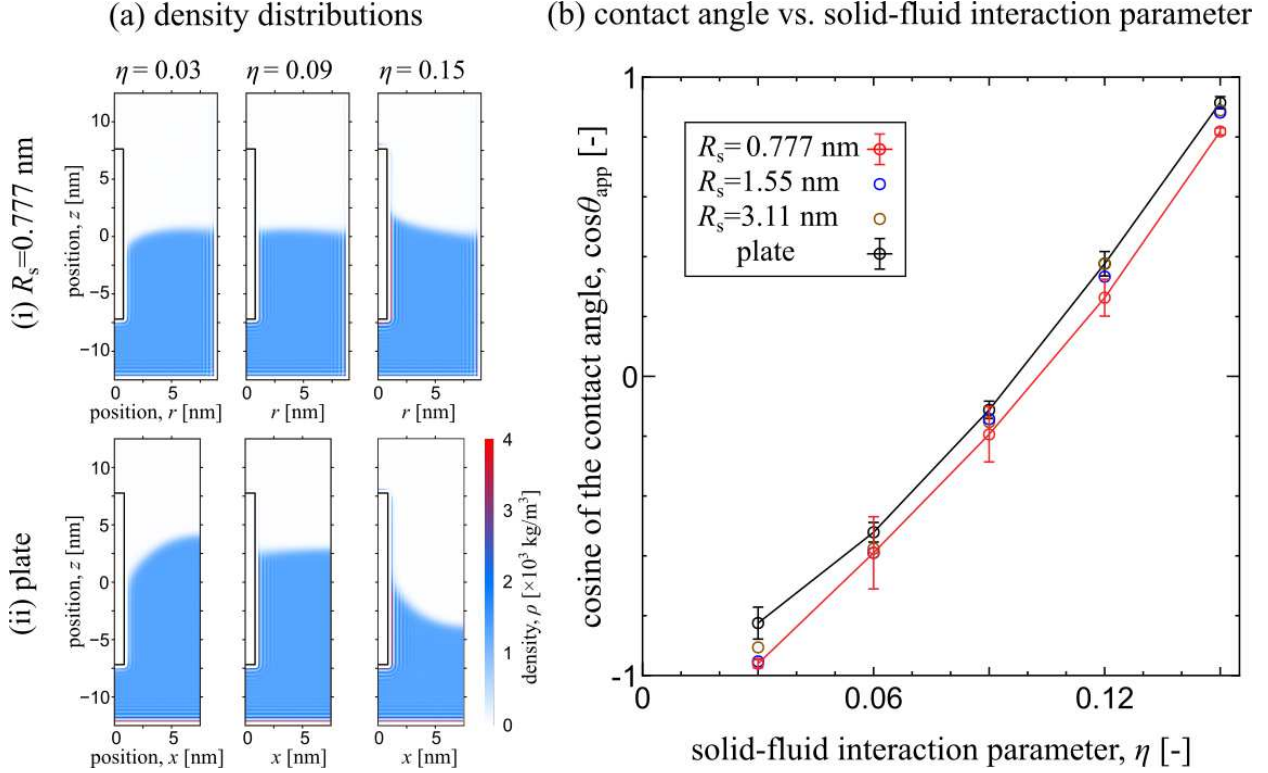


FIG. 3. (a) Density distributions around the (i) solid cylinder of radius $R_s = 0.777$ nm and (ii) plate, and (b) relation between the cosine of contact angle and solid-fluid interaction parameter for different cylinder radii R_s and plate.

bottom of the cylinder to calculate the SL interfacial tension below. The bottom face and the side cylindrical face of the CV are in the liquid bulk, where the former is sufficiently away from both the bottom of the system and bottom of the cylinder, whereas the latter at $r = r_{\text{CV}}$ is away from the side boundary. Analogously, the top face is at the height $z = z_{\text{SL}}$ sufficiently away from both the bottom of the cylinder and the contact line. On the other hand, the concave faces are set at the solid-liquid boundary with its inner side face at $r = r_{\text{SF}}$.

The density distributions around the solid cylinder with the smallest radius $R_s = 0.777$ nm and the plate, and the relation between the SF interaction coefficient η and cosine of the contact angle $\cos \theta_{\text{app}}$ are shown in Fig. 3. For the latter, we displayed the error bars and guide lines only for the plate and for the cylinder systems with $R_s = 0.777$ nm, for better visualization: the error bars for the systems with other radii were comparable to those for $R_s = 0.777$ nm. As seen in Fig. 3 (a), the apparent meniscus shapes of the cylinder

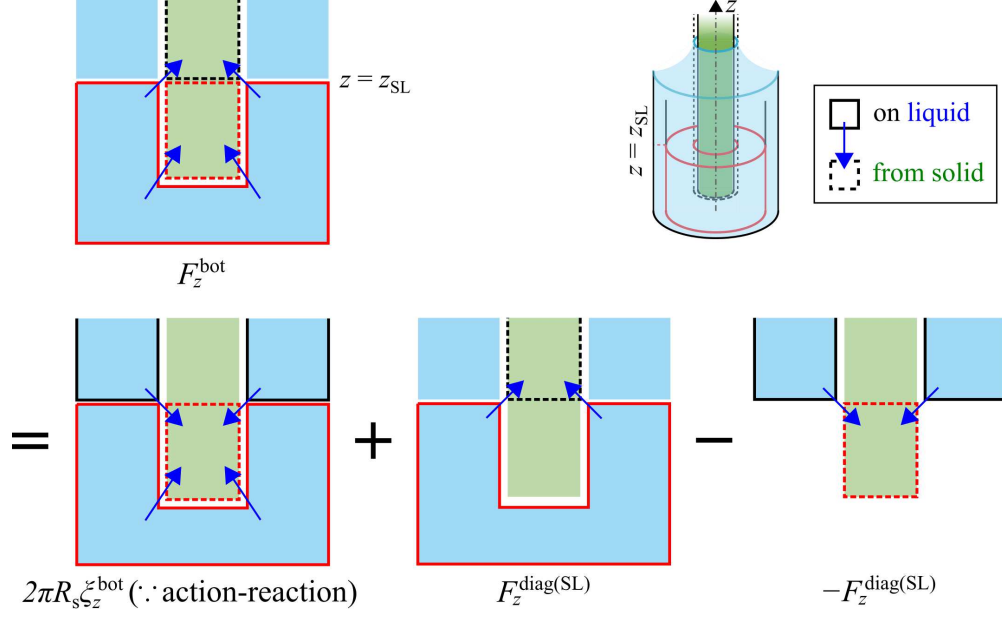


FIG. 4. Schematic of the extraction of the z -direction force from the solid on the fluid in the red control volume around the bottom considering the force distribution in Fig. 2.

and plate are different, indicating that different force balances described by Eqs. (10) and (11), should be adopted to properly evaluate the contact angle from the meniscus shape. With the increase of η , the solid became more wettable, *i.e.*, $\cos \theta_{\text{app}}$ increased, and the cylinder with the smallest Radius $R_s = 0.777$ nm were less wettable, *i.e.*, had smaller $\cos \theta_{\text{app}}$ than the plate for all η values tested. However; we should stress that the radius dependence of the contact angle seen in Fig. 3 (b) was unexpectedly small even with the smallest cylinder with its radius R_s that is comparable to σ_{ff} or σ_{sf} . We discuss the reason in the following with the comparison between the apparent contact angle θ_{app} and the contact angle predicted by Young's equation (1) using the interfacial tensions obtained by the local forces.

B. Curvature dependence of the force around the contact line and the solid-liquid and solid-vapor interfacial tensions

We further investigate the curvature dependence of wetting behavior with the calculations of ξ_z^{cl} and the interfacial tensions. We start from the extraction of the upward force F_z^{bot} exerted from the solid on the liquid in the red control volume (CV) around the bottom

illustrated in the top-left panel of Fig. 4. Note that we evaluate the upward force F_z on the corresponding liquid from the solid as follows: the positive direction for F_z is $+z$ -direction and is opposite to that for ξ_z (force per length) in the $-z$ -direction on the corresponding solid from the liquid. The top face of the CV at $z = z_{\text{SL}}$ is sufficiently away from both the bottom of the solid and the contact line, where the liquid density ρ near the solid is constant in the z -direction satisfying

$$\frac{\partial \rho}{\partial z} = 0 \quad \text{for} \quad (r - R_s)^2 + (z - z_{\text{SL}})^2 \leq (r_c^{\text{sf}})^2, \quad (12)$$

with r_c^{sf} the cut-off distance for solid-fluid interaction. The force of present interest F_z^{bot} comes from the neighbouring solid within the cutoff range, *i.e.*, from the red-dotted and black-dotted solid parts as indicated by the blue arrows (top-left panel). On the other hand, with the condition in Eq. (12), the sum of the upward forces on the liquid parts in the red-solid and black-solid lines from the red-dotted solid part (bottom-left panel) is $2\pi R_s \xi_z^{\text{bot}}$, which is the reaction force on the solid around the bottom indicated in Fig. 2. From the comparison of the arrows regarding the two, F_z^{bot} is obtained by adding the missing force and subtracting the unnecessary force as in the bottom panel as

$$\begin{aligned} F_z^{\text{bot}} &= 2\pi R_s \xi_z^{\text{bot}} + F_z^{\text{diag(SL)}} - (-F_z^{\text{diag(SL)}}) \\ &= 2\pi R_s \xi_z^{\text{bot}} + 2F_z^{\text{diag(SL)}} \end{aligned} \quad (13)$$

where the two “diagonal” forces denoted by $F_z^{\text{diag(SL)}}$ and $-F_z^{\text{diag(SL)}}$ have an opposite sign with the same absolute value due to the symmetry under the condition in Eq. (12).

The value of unknown $F_z^{\text{diag(SL)}}$ now must be determined. Although this $F_z^{\text{diag(SL)}}$ can be obtained directly by MD simulations based on the definition, in the special case where the solid is so smooth compared to the length-scale of solid-fluid inter-particle interaction that the density can be considered constant independent of the position as the present solid with the graphene geometry, $F_z^{\text{diag(SL)}}$ can be analytically expressed by

$$F_z^{\text{diag(SL)}} = -\pi R_s u_{\text{SL}}. \quad (14)$$

The detailed derivation is described in Appendix B. Similarly, the diagonal force $F_z^{\text{diag(SV)}}$ on the vapor below a plane $z = z_{\text{SV}}$ from the solid above the plane can also be analytically formulated by

$$F_z^{\text{diag(SV)}} = -\pi R_s u_{\text{SV}}. \quad (15)$$

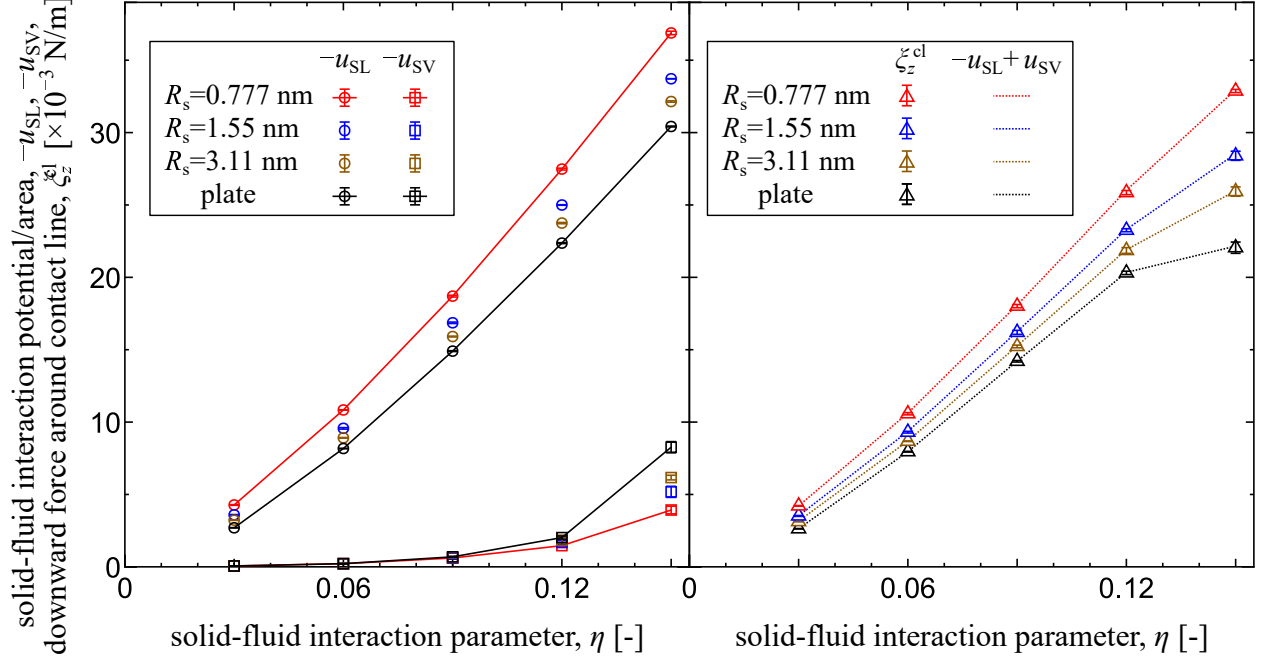


FIG. 5. (Left) dependence SL and SV potential energy densities $-u_{SL}$ and $-u_{SV}$ on the solid-fluid interaction parameter η for solid plate and solid cylinders with different radii R_s . (Right) Comparison between the downward force ξ_z^{cl} on the solid around the CL and the difference of the potential energy density $-u_{SL} + u_{SV}$.

By considering a force balance similar to that illustrated in Fig. 4 and by also assuming that the solid is smooth and the fluid particles are not pinned around the contact line, the downward force on the solid ξ_z^{cl} per length is analytically given by (see Appendix C for details)

$$\xi_z^{cl} = -u_{SL} + u_{SV} = (-u_{SL}) - (-u_{SV}), \quad (16)$$

where the final equality shows that ξ_z^{cl} is the difference in the magnitude between the two interfacial potential energy densities, considering that u_{SL} and u_{SV} are both negative as exemplified in Fig. 2.

Figure 5 shows the dependence of SL and SV potential energy densities $-u_{SL}$ and $-u_{SV}$ on the solid-fluid interaction parameter η for solid plate and solid cylinders with different radii R_s , and the comparison between the downward force ξ_z^{cl} on the solid around the CL and the difference of potential energy density $-u_{SL} + u_{SV}$. As easily expected, $-u_{SL}$ and $-u_{SV}$ increased with the increase of η as shown in the left panel; however, $-u_{SL}$ and $-u_{SV}$ showed opposite dependence on R_s : $-u_{SL}$ was larger for smaller cylinder radius R_s whereas $-u_{SV}$

was smaller. We will discuss this interesting difference later. In the right panel of Fig. 5, a very good agreement between ξ_z^{cl} and $-u_{\text{SL}} + u_{\text{SV}}$ are observed for the whole range of η with different radii R_s in the right panel. This indicates that the force from the solid on the liquid in the CV around the bottom shown as a red concave in Fig. 4 can be properly evaluated by Eq. (14) because the present system with solid particles located at the position of graphene was supposed to be sufficiently smooth to meet the condition assumed in the analytical derivation in Appendices B and C. In addition, due to the opposite radius dependence of $-u_{\text{SL}}$ and $-u_{\text{SV}}$ shown in the left panel, the difference of ξ_z^{cl} for the smallest radius and that for the plate was as large as about 10×10^{-3} N/m, which is comparable to γ_{LV} . In addition, ξ_z^{cl} was much larger than the difference of $-(\gamma_{\text{SL}} - \gamma_{\text{S0}})$ and $-(\gamma_{\text{SV}} - \gamma_{\text{S0}})$ shown later.

We now examine the relative SL interfacial tension by using the total static force balance including the force F_z^{bot} on the red-solid CV in Fig. 4:

$$2\pi \int_{r_{\text{SF}}}^{r_{\text{CV}}} dr \tau_{zz}(r, z_{\text{SL}})r + \pi r_{\text{CV}}^2 p_{\text{L}}^{\text{blk}} + F_z^{\text{bot}} = 0, \quad (17)$$

where the 1st and 2nd terms of the LHS are the fluid stress integral on the top face and pressure from the bottom, respectively. Note that side boundary is set at the bulk satisfying $\tau_{rz} = 0$, and also that the fluid stress is zero on the faces around the concave under the present stress definition.^{3,26,28,63} The first term of the LHS is related to the relative SL interfacial tension $\gamma_{\text{SL}} - \gamma_{\text{S0}}$ with extended Bakker's equation applied for a cylindrical SL interface by (see Appendix A)

$$\gamma_{\text{SL}} - \gamma_{\text{S0}} = \frac{1}{r_{\text{SF}}} \left[\int_{r_{\text{SF}}}^{r_{\text{CV}}} dr \tau_{zz}(r, z_{\text{SL}})r + \frac{(r_{\text{CV}}^2 - r_{\text{SF}}^2)p_{\text{L}}^{\text{blk}}}{2} \right]. \quad (18)$$

Thus, from Eqs. (17), (13) and (18), $\gamma_{\text{SL}} - \gamma_{\text{S0}}$ results in

$$\gamma_{\text{SL}} - \gamma_{\text{S0}} = -\frac{R_s}{r_{\text{SF}}} \xi_z^{\text{bot}} - \frac{r_{\text{SF}}}{2} p_{\text{L}}^{\text{blk}} - \frac{F_z^{\text{diag(SL)}}}{\pi r_{\text{SF}}}, \quad (19)$$

where the pressure $p_{\text{L}}^{\text{blk}}$ was measured in MD systems as the normal force per area exerted on the bottom potential wall for $r \leq r_{\text{CV}}$. Under the condition that Eq. (14) holds for $F_z^{\text{diag(SL)}}$ as in the present systems Eq. (13) is further rewritten by

$$F_z^{\text{bot}} = 2\pi R_s (\xi_z^{\text{bot}} - u_{\text{SL}}), \quad (20)$$

and Eq. (19) writes

$$\gamma_{\text{SL}} - \gamma_{\text{S0}} = -\frac{R_s}{r_{\text{SF}}} \xi_z^{\text{bot}} - \frac{r_{\text{SF}}}{2} p_{\text{L}}^{\text{blk}} + \frac{R_s}{r_{\text{SF}}} u_{\text{SL}}. \quad (21)$$

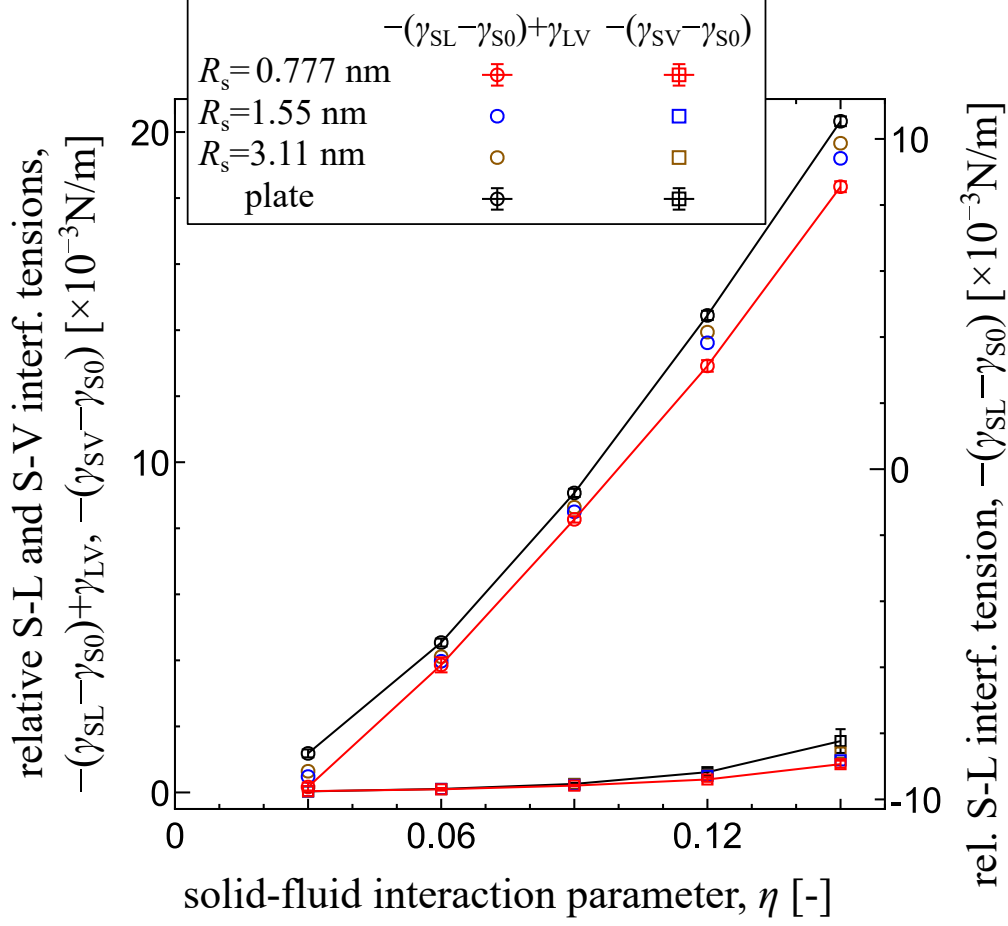


FIG. 6. Dependence of the SL and SV interfacial tensions on the radius of solid cylinders with different wettability.

Similarly, the relative solid-vapor interfacial tension $\gamma_{\text{SV}} - \gamma_{\text{S0}}$ writes

$$\gamma_{\text{SV}} - \gamma_{\text{S0}} = \frac{R_s}{r_{\text{SF}}} \xi_z^{\text{top}} - \frac{r_{\text{SF}}}{2} p_V^{\text{blk}} + \frac{R_s}{r_{\text{SF}}} u_{\text{SV}}. \quad (22)$$

Note that Eqs. (21) and (22) are equivalent to the derivation for the quasi-2D Wilhelmy plate²⁶ except the point that the radii of the solid surface area R_s and solid-fluid interface area r_{SF} are different for the present Wilhelmy-cylinders. Also note that the meniscus shape including the contact angle does not explicitly appear in Eqs. (21) and (22).

Figure 6 shows the relative SL and SV interfacial tensions calculated by Eq. (21) and (22) for different solid radii R_s with various wettability parameter η . For a direct comparison between the two interfacial tensions, the values $-(\gamma_{\text{SL}} - \gamma_{\text{S0}}) + \gamma_{\text{LV}}$ and $-(\gamma_{\text{SV}} - \gamma_{\text{S0}})$ are shown with the left vertical axis, which correspond to the works of adhesion:

$$W_{\text{SL}} \equiv -(\gamma_{\text{SL}} - \gamma_{\text{S0}}) + \gamma_{\text{LV}} \quad (23)$$

and

$$W_{SV} \equiv -(\gamma_{SV} - \gamma_{S0}), \quad (24)$$

where the value of $\gamma_{LV} = 9.79 \times 10^{-3}$ N/m obtained in our previous study²⁶ was used. For a flat interface, they are defined as the minimum works needed to strip the liquid and vapor off the flat solid surface, respectively under constant temperature and pressure condition.^{28,36} Note that both works of adhesion W_{SL} and W_{SV} are positive, and we will discuss about them later from a viewpoint of the free energy as well as the curvature effects. With the decrease of the radius R_s , both $-(\gamma_{SL} - \gamma_{S0})$ and $-(\gamma_{SV} - \gamma_{S0})$ became smaller, and the dependence was more remarkable for larger η value. For the smallest cylinder with $R_s = 0.777$ nm, $-(\gamma_{SL} - \gamma_{S0})$ was about 2×10^{-3} N/m smaller than that of the flat plate. However, $-(\gamma_{SV} - \gamma_{S0})$ was also reduced with the decrease of R_s , and this resulted in the rather small dependence of the contact angle on the radius shown in Fig. 3.

C. Applicability of Young's equation

Using the relative interfacial tensions $\gamma_{SL} - \gamma_{S0}$ and $\gamma_{SV} - \gamma_{S0}$ obtained in the previous subsection, we examined whether Young's equation holds for the present system with a curved solid surface. Figure 7 shows the comparison between the apparent contact angle cosine $\cos \theta_{app}$ in Fig. 3 determined from the meniscus shape and that estimated by Young's equation (1) defined by

$$\begin{aligned} \cos \theta_Y &= \frac{\gamma_{SV} - \gamma_{SL}}{\gamma_{LV}} \equiv \frac{(\gamma_{SV} - \gamma_{S0}) - (\gamma_{SL} - \gamma_{S0})}{\gamma_{LV}} \\ &= \frac{W_{SL} - W_{SV}}{\gamma_{LV}} - 1 \end{aligned} \quad (25)$$

using the interfacial tensions obtained above via the mechanical route. Note that γ_{LV} was set constant considering that its curvature dependence appeared only for a radius of curvature smaller than about $3\sigma_{ff}$ for the LJ fluid,⁵³ which is smaller than that in the present study. In addition, it has been shown that γ_{LV} consistent with Young's equation should be defined at a position excluding the adsorption layers around the SL interface,²⁸ at which the radius of curvature of LV interface is sufficiently large and the curvature effect is negligible. For the whole range of η values and radii R_s tested, $\cos \theta_{app}$ and $\cos \theta_Y$ agreed very well, and this indicates that Young's equation holds for the present systems with curved solid surfaces

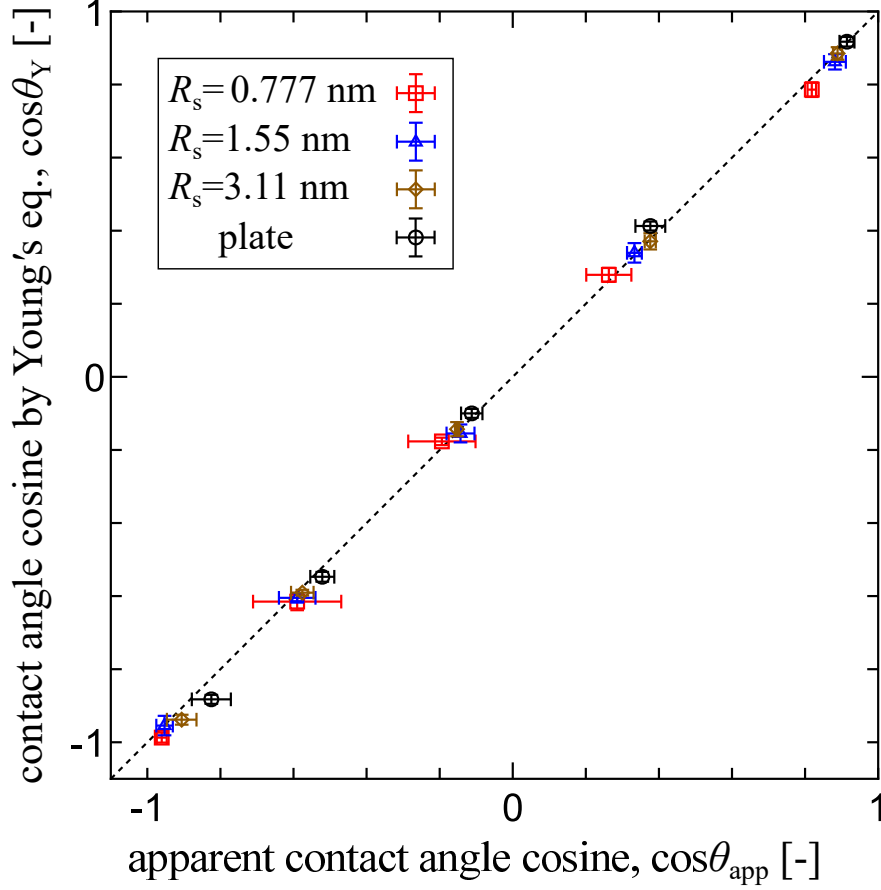


FIG. 7. Comparison between the apparent contact angle $\cos\theta_{\text{app}}$ and that estimated by Young's equation $\cos\theta_Y$ using the interfacial tensions obtained by the mechanical route. The value of η ranges from 0.03 to 0.15 for each cylinder radius R_s and plate.

without pinning if the solid-related relative interfacial tensions $\gamma_{\text{SL}} - \gamma_{\text{S0}}$ and $\gamma_{\text{SV}} - \gamma_{\text{S0}}$ are properly evaluated via a mechanical route.

D. Discussion

A question arises: why was the curvature dependence of the relative interfacial tensions $\gamma_{\text{SL}} - \gamma_{\text{S0}}$ and $\gamma_{\text{SV}} - \gamma_{\text{S0}}$ shown in Fig. 6 not so large compared to the contact line force $\xi_z^{\text{cl}} = -u_{\text{SL}} + u_{\text{SV}}$ seen in Fig. 5? More specifically, why did $-u_{\text{SL}}$ in the left panel of Fig. 5 and $-(\gamma_{\text{SL}} - \gamma_{\text{S0}})$ in Fig. 6 show opposite dependence on R_s ? To examine the curvature dependence of $-u_{\text{SL}}$, we evaluated the density field around the solid-liquid interface, where we have carried out an additional simulation with a solid cylinder with a chiral index (60,0)

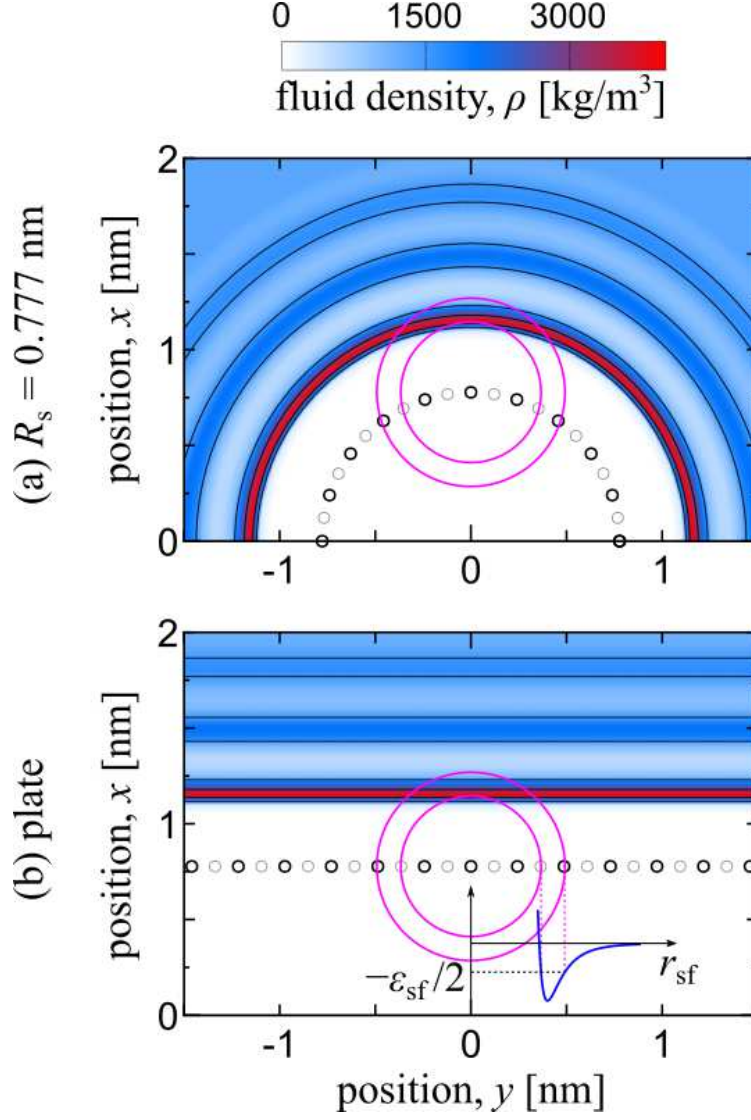


FIG. 8. Comparison of the fluid-density around a solid-liquid interface between the (a) cylinder with $R_s = 0.777$ nm and (b) flat plate, with $\eta = 0.15$. Positions of the solid particles are shown with small black and gray circles, and the distance range of r_{sf} from a solid particle satisfying interaction potential $\Phi_{sf}(r_{sf}) \leq -\epsilon_{sf}/2$ is depicted by magenta circles.

($R_s = 2.33$ nm). Figure 8 shows the comparison of the fluid-density around a solid-liquid interface between the (a) cylinder with $R_s = 0.777$ nm and (b) flat plate, with $\eta = 0.15$. Positions of the solid particles are shown with small black and gray circles, where the particles with the same color are at the same height z , and the distance range of r_{sf} from a black solid particle satisfying interaction potential $\Phi_{sf}(r_{sf}) \leq -\epsilon_{sf}/2$, as indicated by the blue potential graph, is depicted by magenta circles. As seen in this figure, high density region in red

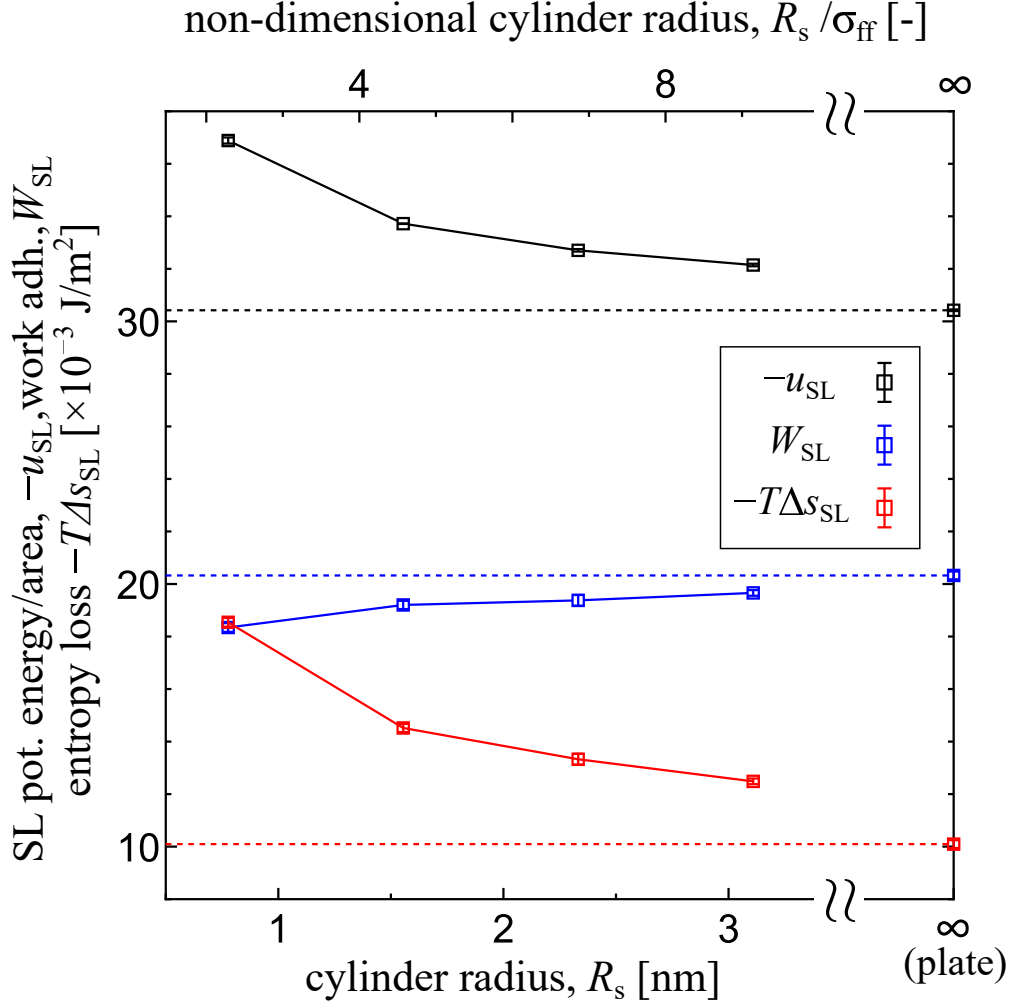


FIG. 9. Solid-liquid interfacial potential energy per area $-u_{SL}$, the work of adhesion W_{SL} , and the entropy loss $-T\Delta s_{SL}$ calculated by Eq. (26) for various cylinder radius R_s with a solid-fluid interaction parameter $\eta = 0.15$.

corresponding to the fluid first adsorption layer are included in this distance range more for $R_s = 0.777$ nm, and this results in the higher $-u_{SL}$ for smaller R_s indicated in the left panel of Fig. 5 because the fluid particles in this distance range have the main contribution. Similarly, one can expect smaller $-u_{SV}$ for smaller R_s because the fluid particles at the SV interface are simply adsorbed on the solid surface as a single particle, *i.e.*, these fluid particles do not form adsorption layers as those around the SL interface observed in Fig. 2, and such single particle is subject to weaker interaction potential from the curved solid than from the flat solid.

Different from the average SL interaction potential $-u_{SL}$, the relative interfacial tension

is considered the interfacial free energy per area, *i.e.*, $\gamma_{\text{SL}} - \gamma_{\text{S0}}$ is related to the SL work of adhesion W_{SL} in Eq. (23), and it consists of internal energy and entropy terms:^{35,36}

$$W_{\text{SL}} = -(\gamma_{\text{SL}} - \gamma_{\text{S0}}) + \gamma_{\text{LV}} = -u_{\text{SL}} - (-T\Delta s_{\text{SL}}), \quad (26)$$

where $-T\Delta s_{\text{SL}}$ is due to the entropy “loss” $-\Delta s_{\text{SL}}$ induced by the density increase in the adsorption layers of the SL interface. Figure 9 shows the solid-liquid interfacial potential energy per area $-u_{\text{SL}}$, the work of adhesion W_{SL} and the entropy loss $-T\Delta s_{\text{SL}}$ in Eq. (26) for various cylinder radius R_{s} with $\eta = 0.15$. Note that the additional data for a cylinder radius $R_{\text{s}} = 2.33$ nm were also shown, and the radius for the plate was set as $R_{\text{s}} = \infty$. A larger entropy loss exceeding the potential gain in $-u_{\text{SL}}$ resulted in the opposite curvature dependence between the SL interfacial potential energy $-u_{\text{SL}}$ and the relative interfacial tension $-(\gamma_{\text{SL}} - \gamma_{\text{S0}})$ seen in Figs. 5 and 6. In addition, it is indicated that the curvature effect could remain even for a relatively large cylinder radius R_{s} larger than about $10\sigma_{\text{ff}}$, which is much larger than the radius dependence range of γ_{LV} reported for the LJ droplets.⁵³

IV. CONCLUDING REMARKS

In this study, we successfully extracted the SL and SV interfacial tensions of a simple Lennard-Jones fluid around a solid cylinder with a nanometer-scale diameter by extending the theoretical nano-Wilhelmy equations for a quasi-two-dimensional flat solid plate from our previous study. The SL and SV interfacial tensions were calculated from the integral of the normal-stress in the wall-tangential direction by considering the mechanical force balances on control volumes set around the bottom and top of the solid cylinder subject to the fluid stress and external force from the solid, where the local force on the solid around the contact line expressed by these external forces agreed well with the analytical expression. The theoretical contact angle calculated by Young’s equation using these interfacial tensions agreed well with the apparent contact angle estimated by the analytical solution fitted to the meniscus shape, showing that Young’s equation holds even for menisci around solids with nanoscale curvature if the interfacial tensions are properly evaluated. It was also shown that the curvature dependence of the SL and SV interfacial tensions as the free energy was different from that of the corresponding interaction potential energies as a part of the internal energy, which explains the weak curvature dependence of the contact angle in the present results.

The accurate calculation of the interfacial tensions on curved surfaces could explain the unique wetting behavior of water on carbon nanotubes.^{47,48} In addition, it should enable the exploration of the Tolman equation for the solid-related interfaces. Related to this, an interesting future target is the interfacial tensions inside the curved interface from a mechanical route, which should enable the analysis of nano-confinement effects or nanoscale capillary as well, *e.g.*, in carbon nanotubes.

ACKNOWLEDGMENTS

T.O., H.K. and Y.Y. were supported by JSPS KAKENHI grant (Nos. JP18K03929, JP20J20251 and JP18K03978), Japan, respectively. Y.Y. was also supported by JST CREST grant (No. JPMJCR18I1), Japan.

DATA AVAILABILITY

The data that support the findings of this study are available from the corresponding author upon reasonable request.

AUTHOR DECLARATIONS

Conflict of Interest

The authors have no conflicts to disclose.

Appendix A: Extended Bakker's equation for cylinder

We formulate the relative solid-liquid (SL) interfacial tension relative to the solid-vacuum (S0) $\gamma_{\text{SL}} - \gamma_{\text{S0}}$ between cylindrical solid surface and liquid through the thought experiment shown in Fig. 10. The side piston normal to the cylinder axis z is in contact only with the liquid, *i.e.*, the inner radius is at r_{SL} set at the limit radius nearest to the solid that the fluid particle can reach, whereas the outer radius $r_{\text{L}}^{\text{blk}}$ is at liquid bulk sufficiently away from the SL interface. The axis-normal stress defined by

$$\tau_{zz}(r) \equiv -p_z(r) \tag{A1}$$

is a function of radial position r , and it satisfies

$$p_z(r) = p_{\text{L}}^{\text{blk}} = \text{const.} \quad (r \geq r_{\text{L}}^{\text{blk}}). \tag{A2}$$

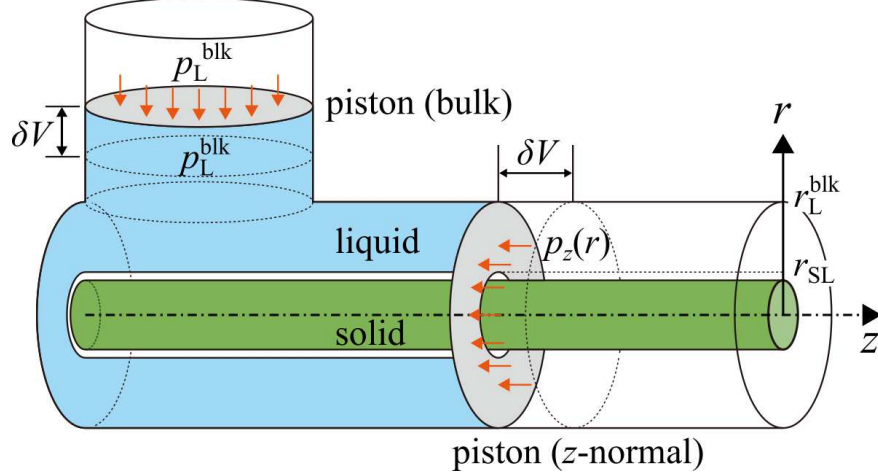


FIG. 10. Thought experiment for the connection between relative solid-liquid interfacial tension and pressure distribution around the solid cylinder.

On the other hand, the top piston is set at the liquid bulk, on which homogeneous pressure identical to the bulk pressure p_L^{blk} is exerted. We suppose a virtual infinitesimal displacement δz of the side piston with a simultaneous downward displacement of the top piston so that the liquid volume may not change. If the operation is quasi-static at a constant temperature, the change of the Helmholtz free energy δF is equal to the work δW exerted on the system given by

$$\delta F = \delta W = p_L^{\text{blk}} \delta V - 2\pi \delta z \int_{r_{\text{SL}}}^{r_L^{\text{blk}}} dr p_z(r) r \quad (\text{A3})$$

where the volume increase and decrease δV due to the motions of side and top pistons, respectively writes

$$\delta V = 2\pi \delta z \int_{r_{\text{SL}}}^{r_L^{\text{blk}}} dr r = \pi [(r_L^{\text{blk}})^2 - r_{\text{SL}}^2] \delta z \quad (\text{A4})$$

The free energy change δF in Eq. (A3) is uniquely defined as long as r_L^{blk} is set in the bulk satisfying Eq. (A2). From a macroscopic point of view, the SL interface is increased and S0 interface is reduced with this operation. By assuming that the SL interface is at r_{SL} , it follows that

$$\delta F = 2\pi r_{\text{SL}} (\gamma_{\text{SL}} - \gamma_{\text{S0}}) \delta z \quad (\text{A5})$$

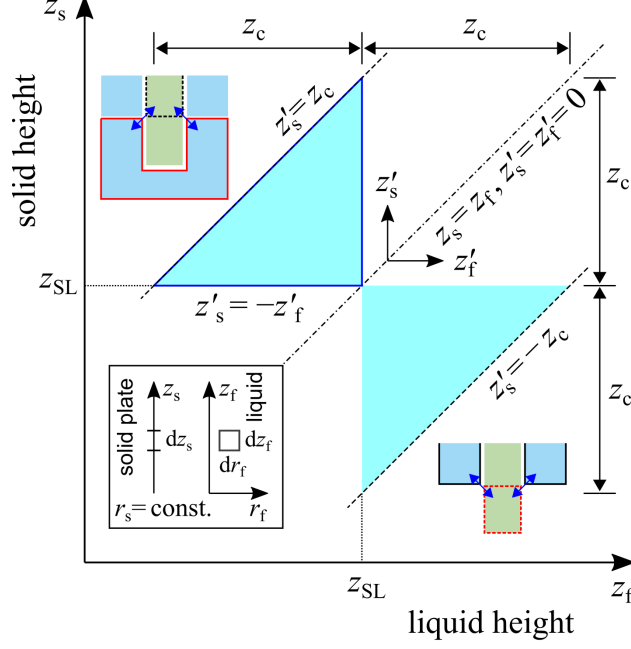


FIG. 11. Region for the double integral of the mean field to calculate the interaction between the solid cylinder above $z_s = z^{\text{SL}}$ and liquid below $z_f = z^{\text{SL}}$ (top-left triangle in solid blue line). The geometrical relation is shown in the inset. The cutoff distance z_c for $|z_f - z_s|$ depends on the relative radial position $r_f - R_s$.

By equating Eqs. (A3) and (A5), the following relation is derived as extended Bakker's equation for a cylindrical SL interface:

$$\gamma_{\text{SL}} - \gamma_{\text{S0}} = \frac{1}{r_{\text{SL}}} \left[\int_{r_{\text{SL}}}^{r_{\text{L}}^{\text{blk}}} dr \tau_{zz}(r)r + \frac{p_{\text{L}}^{\text{blk}} [(r_{\text{L}}^{\text{blk}})^2 - r_{\text{SL}}^2]}{2} \right], \quad (\text{A6})$$

where Eq. (A1) is used as well. Equation (A6) means that the relative SL interfacial tension is obtained with the stress integral, bulk pressure and the interface position.

The relative solid-vapor (SV) interfacial tension is expressed as well by

$$\gamma_{\text{SV}} - \gamma_{\text{S0}} = \frac{1}{r_{\text{SV}}} \left[\int_{r_{\text{SV}}}^{r_{\text{V}}^{\text{blk}}} dr \tau_{zz}(r)r + \frac{p_{\text{V}}^{\text{blk}} [(r_{\text{V}}^{\text{blk}})^2 - r_{\text{SV}}^2]}{2} \right]. \quad (\text{A7})$$

Appendix B: Extraction of the interaction force between the liquid and solid across a z -normal plane at a SL interface.

We derive the interaction force $F_z^{\text{diag(SL)}}$ exemplified in the bottom panels of Fig. 4, namely, the interaction force between the solid above a z -normal plane $z = z_{\text{SL}}$ and liquid

below that plane. The plane $z = z_{\text{SL}}$ is at a height around which the fluid density is independent of the position z because the plane is sufficiently away from the contact line and the bottom of the cylinder.

Taking into account that the solid is supposed to be smooth for the fluid particles because the interparticle distance parameters σ_{ff} and σ_{sf} are sufficiently large compared to r_{ss} between solid particles, the solid-liquid interaction force can be analytically modeled by assuming the mean fields of the fluid and solid. The mean number density per volume $\rho_V^{\text{f}}(r_{\text{f}})$ ($= \rho/m_{\text{f}}$) of the fluid is given as a function of the radial position r_{f} of the fluid, whereas a constant mean number density per area ρ_A^{s} of the solid at $r = R_{\text{s}}$ is used considering the present system with a solid cylinder of zero-thickness without volume; however, the following derivation can easily be extended for a system with a solid with a volume and density per volume in the range $r \leq R_{\text{s}}$.

We start from the potential energy on a solid particle at position $(R_{\text{s}}, \vartheta_{\text{s}}, z_{\text{s}})$ due to a fluid particle at $(r_{\text{f}}, \vartheta_{\text{f}}, z_{\text{f}})$ both in the cylindrical $r\vartheta z$ -coordinate, given by Eq. (2). Assuming that the fluid particles are homogeneously distributed in the azimuth direction ϑ with a number density $\rho_V^{\text{f}}(r_{\text{f}}, z_{\text{f}})$ per volume, the mean potential field from an infinitesimal fluid volume segment of $dz_{\text{f}} \times 2\pi r_{\text{f}} dr_{\text{f}}$ on a solid particle is defined by using $\rho_V^{\text{f}}(z_{\text{f}}, r_{\text{f}})$ and the mean local potential $\phi(z'_{\text{f}}, r'_{\text{f}})$ as $\rho_V^{\text{f}}(z_{\text{f}}, x_{\text{f}}) dz_{\text{f}} dr_{\text{f}} \cdot \phi(z'_{\text{f}}, r'_{\text{f}})$, where $\phi(z'_{\text{f}}, r'_{\text{f}})$ is given by

$$\phi(z'_{\text{f}}, r'_{\text{f}}) \equiv \int_0^{2\pi} \Phi_{\text{LJ}}(r_{\text{sf}}) r_{\text{f}} d\vartheta_{\text{f}} \quad (\text{B1})$$

where we define

$$r_{\text{sf}} = \sqrt{(r_{\text{f}} \cos \vartheta_{\text{f}} - R_{\text{s}} \cos \vartheta_{\text{s}})^2 + (r_{\text{f}} \sin \vartheta_{\text{f}} - R_{\text{s}} \sin \vartheta_{\text{s}})^2 + z'_{\text{f}}^2}, \quad (\text{B2})$$

and

$$z'_{\text{f}} \equiv z_{\text{f}} - z_{\text{s}} \equiv -z'_{\text{s}}, \quad r'_{\text{f}} \equiv r_{\text{f}} - R_{\text{s}}. \quad (\text{B3})$$

Then, the local force in the z -direction $f_z^{\text{s}}(z'_{\text{f}}, r'_{\text{f}}) dz_{\text{f}} dr_{\text{f}} dz_{\text{s}}$ exerted on the solid cylinder in $[z_{\text{s}}, z_{\text{s}} + dz_{\text{s}}]$ with an area number density of the solid particles $\rho_A^{\text{s}}(z_{\text{s}})$ from the present fluid volume-segment is given by:

$$f_z^{\text{s}}(z_{\text{s}}, z_{\text{f}}, r_{\text{f}}) dz_{\text{f}} dr_{\text{f}} dz_{\text{s}} = -\rho_V^{\text{f}}(z_{\text{f}}, r_{\text{f}}) \frac{\partial \phi(z'_{\text{f}}, r'_{\text{f}})}{\partial z_{\text{s}}} dz_{\text{f}} dr_{\text{f}} \cdot 2\pi R_{\text{s}} \rho_A^{\text{s}}(z_{\text{s}}) dz_{\text{s}} \quad (\text{B4})$$

where

$$f_z^{\text{s}}(z_{\text{s}}, z_{\text{f}}, r_{\text{f}}) = -2\pi R_{\text{s}} \rho_A^{\text{s}}(z_{\text{s}}) \rho_V^{\text{f}}(z_{\text{f}}, r_{\text{f}}) \frac{\partial \phi(z'_{\text{f}}, r'_{\text{f}})}{\partial z_{\text{s}}} \quad (\text{B5})$$

denotes the axial force density on the solid given as a function of z_s , z_f and r_f .

Since $\Phi_{\text{LJ}}(r_{\text{sf}})$ is truncated at the cutoff distance r_c in the present case,

$$\begin{aligned} \phi(z'_f, r'_f) &= 0, \quad \frac{\partial \phi(z'_f, r'_f)}{\partial z_s} = 0 \\ \text{for } |z'_f| &\geq \sqrt{r_c^2 - r'^2_f} \equiv z_c(r'_f) \quad \text{or} \quad r'_f \geq r_c \end{aligned} \quad (\text{B6})$$

holds, where $z_c(r'_f)$ as a function of r'_f denotes the cutoff with respect to z'_f . This cutoff is not critical as long as $\phi(z'_f, r'_f)$ quickly vanishes with the increase of r , but we continue the derivation including the cutoff for simplicity. With the definition of r_{SF} as the limit that the fluid could reach, it follows that

$$\rho_V^f = 0 \quad \text{for } r_f < r_{\text{SF}}. \quad (\text{B7})$$

In addition, considering that $\phi(z'_f, r'_f)$ is an even function with respect to z'_f , *i.e.*,

$$\phi(z'_f, r'_f) = \phi(-z'_f, r'_f), \quad (\text{B8})$$

it follows for the mean local potential ϕ that

$$\frac{\partial \phi(z'_f, r'_f)}{\partial z_s} = -\frac{\partial \phi(-z'_f, r'_f)}{\partial z_s}, \quad (\text{B9})$$

and

$$\frac{\partial \phi(z'_f, r'_f)}{\partial z_s} = -\frac{\partial \phi(z'_f, r'_f)}{\partial z_f}, \quad (\text{B10})$$

where Eq. (B3) is applied for the latter. This corresponds to the action-reaction relation between solid and fluid particles under a simple two-body interaction, *i.e.*,

$$f_z^f(z_s, z_f, r_f) = -f_z^s(z_s, z_f, r_f) = -2\pi R_s \rho_A^s(z_s) \rho_V^f(z_f, r_f) \frac{\partial \phi(z'_f, r'_f)}{\partial z_f} \quad (\text{B11})$$

holds for the tangential force density on the fluid f_z^f .

Based on these properties, we now derive the analytical expression of the force exerted on the solid above a z -normal plane $z = z_{\text{SL}}$ from the liquid below that plane, *i.e.*, the force of interest $F_z^{\text{diag(SL)}}$ given by

$$\begin{aligned} F_z^{\text{diag(SL)}} &= \int_0^{r_c} dr'_f \int_{-z_c(r'_f)}^0 dz'_f \int_{-z'_f}^{z_c(r'_f)} dz'_s f_z^f \\ &= - \int_0^{r_c} dr'_f \left[\int_{-z_c(r'_f)}^0 dz'_f \left(\int_{-z'_f}^{z_c(r'_f)} dz'_s f_z^s \right) \right], \end{aligned} \quad (\text{B12})$$

where the double integral in the square brackets corresponds to the top-left region in Fig. 11. Let the density ρ_V^f for $z_{\text{SL}} - z_c < z_f < z_{\text{SL}} + z_c$ be given as a unique function of r_f by

$$\rho_V^f(z_f, r_f) = \rho_V^{f(\text{SL})}(r_f). \quad (\text{B13})$$

Then, it follows for the double integral in the square brackets in Eq. (B12) that

$$\begin{aligned} & \int_{-z_c}^0 dz'_f \left(\int_{-z'_f}^{z_c} dz'_s f_z^s \right) \\ &= -2\pi R_s \int_{-z_c}^0 dz'_f \rho_V^{f(\text{SL})}(r'_f) \left[\int_{-z'_f}^{z_c} dz'_s \rho_A^s(z_s) \frac{\partial \phi(z'_f, r'_f)}{\partial z_s} \right] \\ &= -2\pi R_s \int_{-z_c}^0 \rho_V^{f(\text{SL})}(r'_f) dz'_f \left\{ [\rho_A^s(z_s) \phi(z'_f, r'_f)]_{z'_s=-z'_f}^{z_c} - \int_{-z'_f}^{z_c} dz'_s \frac{d\rho_A^s(z_s)}{dz_s} \phi(z'_f, r'_f) \right\} \\ &= 2\pi R_s \int_{-z_c}^0 dz'_f \rho_V^{f(\text{SL})}(r'_f) \left[\rho_A^s(-z'_f) \phi(-z'_f, r'_f) + \int_{-z'_f}^{z_c} dz'_s \frac{d\rho_A^s(z_s)}{dz_s} \phi(z'_f, r'_f) \right], \\ &= 2\pi R_s \int_{-z_c}^0 dz'_f \rho_V^{f(\text{SL})}(r'_f) \rho_A^s(-z'_f) \phi(z'_f, r'_f) \\ &+ 2\pi R_s \int_{-z_c}^0 dz'_f \rho_V^{f(\text{SL})}(r'_f) \left[\int_{-z'_f}^{z_c} dz'_s \frac{d\rho_A^s(z_s)}{dz_s} \phi(z'_f, r'_f) \right] \end{aligned} \quad (\text{B14})$$

where $\phi(z_c, r'_f) = 0$ and Eq. (B8) are used for the 4th equality.

With an additional assumption of

$$\rho_A^s = \text{const.}, \quad (\text{B15})$$

the 2nd term of the right-most HS becomes zero, and it follows

$$\begin{aligned} \int_{-z_c}^0 dz'_f \left(\int_{-z'_f}^{z_c} dz'_s f_z^s \right) &= 2\pi R_s \rho_A^s \int_{-z_c}^0 dz'_f \rho_V^{f(\text{SL})}(r'_f) \phi(z'_f, r'_f) \\ &= \pi R_s \rho_A^s \int_{-z_c}^{z_c} dz'_f \rho_V^{f(\text{SL})}(r'_f) \phi(z'_f, r'_f) \end{aligned} \quad (\text{B16})$$

considering that ϕ is an even function with respect to z'_f for the second equality. By inserting Eq. (B16) into Eq. (B12), it follows

$$F_z^{\text{diag}(\text{SL})} = -\pi R_s \rho_A^s \int_0^{r_c} dr'_f \int_{-z_c(r'_f)}^{z_c(r'_f)} dz'_f \rho_V^{f(\text{SL})}(r'_f) \phi(z'_f, r'_f) \quad (\text{B17})$$

Indeed, the RHS of Eq. (B17) can be expressed using the following SL potential energy density u_{SL} given by

$$u_{\text{SL}} \equiv \rho_A^s \int_0^{r_c} dr'_f \int_{-z_c(r'_f)}^{z_c(r'_f)} dz'_f \rho_V^{f(\text{SL})}(r'_f) \phi(z'_f, r'_f) \quad (\text{B18})$$

which represents the SL potential energy per solid area at the SL interface away both from the CL and from the bottom of the solid plate. With u_{SL} , Eq. (B17) writes

$$F_z^{\text{diag(SL)}} = -\pi R_s u_{\text{SL}} \quad (\text{B19})$$

which corresponds to Eq. (14) in the main text.

Similar to $F_z^{\text{diag(SL)}}$, the interaction force $F_z^{\text{diag(SV)}}$ between the solid above a z -normal plane $z = z_{\text{SV}}$ and the vapor below that plane writes

$$F_z^{\text{diag(SV)}} = -\pi R_s u_{\text{SV}}, \quad (\text{B20})$$

where the SV potential energy density u_{SV} is given by

$$u_{\text{SV}} \equiv \rho_A^s \int_0^{r_c} dr'_f \rho_V^{\text{f(SV)}}(r'_f) \int_{-z_c(r'_f)}^{z_c(r'_f)} dz'_f \phi(z'_f, r'_f). \quad (\text{B21})$$

Appendix C: Extraction of the force exerted on the solid around the contact line.

We can formulate the downward force on the solid around the contact line $2\pi R_s \xi_z^{\text{cl}}$ from the fluid as the reaction force, *i.e.*, the upward force on the liquid from the solid, from the force balance similar to that displayed in Fig. 4. Let F_z^{cl} be the force on the liquid around the contact line, $2\pi R_s \xi_z^{\text{cl}}$ can be obtained by adding $F_z^{\text{diag(SL)}} - F_z^{\text{diag(SV)}}$ and subtracting $-F_z^{\text{diag(SL)}} + F_z^{\text{diag(SV)}}$ as

$$2\pi R_s \xi_z^{\text{cl}} = F_z^{\text{cl}} + 2(F_z^{\text{diag(SL)}} - F_z^{\text{diag(SV)}}) \quad (\text{C1})$$

as illustrated in Fig. 12. In case the solid surface is smooth and flat and no pinning is induced,

$$F_z^{\text{cl}} = 0 \quad (\text{C2})$$

holds because the average surface lateral force on each fluid particles from the solid is zero.^{26,28,29,36} This condition is applicable to the present systems. By inserting Eqs. (14), (15) and (C2) into Eq. (C1),

$$\xi_z^{\text{cl}} = -u_{\text{SL}} + u_{\text{SV}} = (-u_{\text{SL}}) - (-u_{\text{SV}}) \quad (\text{C3})$$

is derived as the analytical expression of ξ_z^{cl} in Eq. (16) in the main text, where the final expression is to emphasize that the potential energy densities u_{SL} and u_{SV} are both negative.

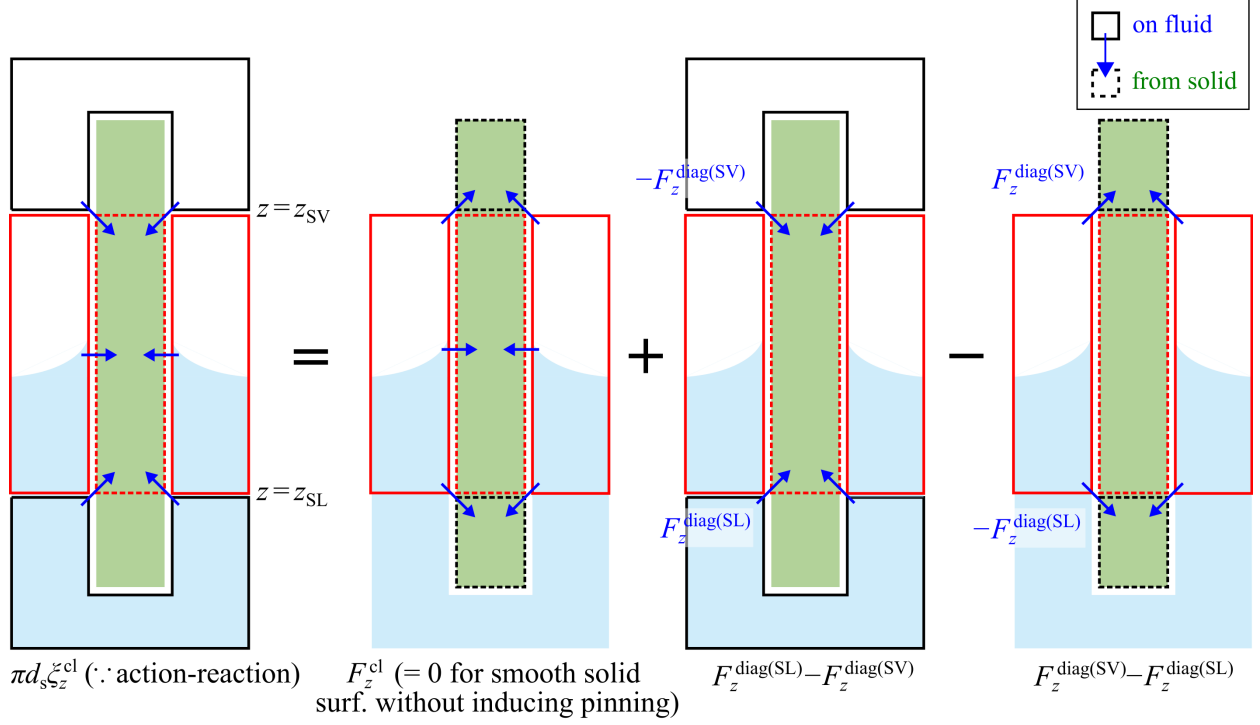


FIG. 12. Schematic of the extraction of the z -direction force on the solid around the contact line from the fluid.

REFERENCES

- ¹P.-G. de Gennes, ““Wetting” Statics and dynamics,” *Rev. Mod. Phys.* **57**, 827–863 (1985).
- ²S. Ono and S. Kondo, *Molecular Theory of Surface Tension in Liquids*, *Encyclopedia of Physics / Handbuch der Physik* (Springer, 1960) pp. 134–280.
- ³J. S. Rowlinson and B. Widom, *Molecular Theory of Capillarity* (Dover, 1982).
- ⁴L. Schimmele, M. Naplórkowski, and S. Dietrich, “Conceptual aspects of line tensions,” *J. Chem. Phys.* **127** (2007), 10.1063/1.2799990, 0703821 [cond-mat].
- ⁵J. W. Drelich, L. Boinovich, E. Chibowski, C. D. Volpe, L. Holysz, A. Marmur, and S. Siboni, “Contact angles: History of over 200 years of open questions,” *Surf. Innov.*, 1–25 (2019).
- ⁶T. Young, “An essay on the cohesion of fluids,” *Phil. Trans. R. Soc. Lond.* **95**, 65 (1805).
- ⁷L. Gao and T. J. McCarthy, “Wetting 101°,” *Langmuir* **25**, 14105–14115 (2009).
- ⁸M. N. Popescu, G. Oshanin, S. Dietrich, and A. M. Cazabat, “Precursor films in wetting phenomena,” *Journal of Physics: Condensed Matter* **24**, 243102 (2012).

- ⁹L. R. White, “On deviations from Young’s equation,” J. Chem. Soc., Faraday Trans. 1 **73**, 390–398 (1977).
- ¹⁰L. Boruvka and A. W. Neumann, “Generalization of the classical theory of capillarity,” J. Chem. Phys. **66**, 5464–5476 (1977).
- ¹¹A. Marmur, “Line tension and the intrinsic contact angle in solid–liquid–fluid systems,” J. Colloid Interface Sci. **186**, 462–466 (1997).
- ¹²V. K. Kumikov and K. B. Khokonov, “On the measurement of surface free energy and surface tension of solid metals,” J. Appl. Phys. **54**, 1346–1350 (1983).
- ¹³W. R. Tyson and W. A. Miller, “Surface free energies of solid metals: Estimation from liquid surface tension measurements,” Surface Science **62**, 267 – 276 (1977).
- ¹⁴J. G. Kirkwood and F. P. Buff, “The statistical mechanical theory of surface tension,” J. Chem. Phys. **17**, 338–343 (1949).
- ¹⁵G. Bakker, Kapillarität und Oberflächenspannung, Vol. 6 (Wien-Harms, 1928).
- ¹⁶M. P. Allen and D. J. Tildesley, Computer Simulation of Liquids (Oxford University Press, 1987).
- ¹⁷J. Z. Tang and J. G. Harris, “Fluid wetting on molecularly rough surfaces,” J. Chem. Phys. **103**, 8201–8208 (1995).
- ¹⁸G. J. Gloor, G. Jackson, F. J. Blas, and E. De Miguel, “Test-area simulation method for the direct determination of the interfacial tension of systems with continuous or discontinuous potentials,” J. Chem. Phys. **123**, 134703 (2005).
- ¹⁹T. Ingebrigtsen and S. Toxvaerd, “Contact angles of Lennard-Jones liquids and droplets on planar surfaces,” J. Phys. Chem. C **111**, 8518–8523 (2007).
- ²⁰S. K. Das and K. Binder, “Does Young’s equation hold on the nanoscale? A Monte Carlo test for the binary Lennard-Jones fluid,” Europhy. Lett. **92**, 26006 (2010).
- ²¹J. H. Weijs, A. Marchand, B. Andreotti, D. Lohse, and J. H. Snoeijer, “Origin of line tension for a Lennard-Jones nanodroplet,” Phys. Fluids **23**, 022001 (2011).
- ²²D. Seveno, T. D. Blake, and J. de Coninck, “Young’s equation at the nanoscale,” Phys. Rev. Lett. **111**, 096101 (2013).
- ²³M. J. P. Nijmeijer and J. M. J. van Leeuwen, “Microscopic expressions for the surface and line tension,” J. Phys. A: Math. Gen. **23**, 4211–4235 (1990).
- ²⁴M. J. P. Nijmeijer, C. Bruin, A. F. Bakker, and J. M. J. van Leeuwen, “Wetting and drying of an inert wall by a fluid in a molecular-dynamics simulation,” Phys. Rev. A **42**,

- 6052–6059 (1990).
- ²⁵S. Nishida, D. Surblys, Y. Yamaguchi, K. Kuroda, M. Kagawa, T. Nakajima, and H. Fujimura, “Molecular dynamics analysis of multiphase interfaces based on *in situ* extraction of the pressure distribution of a liquid droplet on a solid surface,” J. Chem. Phys. **140**, 074707 (2014).
- ²⁶Y. Imaizumi, T. Omori, H. Kusudo, C. Bistafa, and Y. Yamaguchi, “Wilhelmy equation revisited: A lightweight method to measure liquid–vapor, solid–liquid, and solid–vapor interfacial tensions from a single molecular dynamics simulation,” J. Chem. Phys. **153**, 034701 (2020), 2004.14248.
- ²⁷D. Surblys, Y. Yamaguchi, K. Kuroda, M. Kagawa, T. Nakajima, and H. Fujimura, “Molecular dynamics analysis on wetting and interfacial properties of water-alcohol mixture droplets on a solid surface,” J. Chem. Phys. **140**, 034505 (2014).
- ²⁸Y. Yamaguchi, H. Kusudo, D. Surblys, T. Omori, and G. Kikugawa, “Interpretation of Young’s equation for a liquid droplet on a flat and smooth solid surface: Mechanical and thermodynamic routes with a simple Lennard-Jones liquid,” J. Chem. Phys. **150**, 044701 (2019).
- ²⁹H. Kusudo, T. Omori, and Y. Yamaguchi, “Extraction of the equilibrium pinning force on a contact line exerted from a wettability boundary of a solid surface through the connection between mechanical and thermodynamic routes,” J. Chem. Phys. **151**, 154501 (2019).
- ³⁰F. Leroy, D. J. V. A. Dos Santos, and F. Müller-Plathe, “Interfacial excess free energies of solid-liquid interfaces by molecular dynamics simulation and thermodynamic integration,” Macromol. Rapid Commun. **30**, 864–870 (2009).
- ³¹F. Leroy and F. Müller-Plathe, “Solid-liquid surface free energy of Lennard-Jones liquid on smooth and rough surfaces computed by molecular dynamics using the phantom-wall method,” J. Chem. Phys. **133**, 044110 (2010).
- ³²F. Leroy and F. Müller-Plathe, “Dry-surface simulation method for the determination of the work of adhesion of solid–liquid interfaces,” Langmuir **31**, 8335–8345 (2015).
- ³³M. Kanduč and R. R. Netz, “Atomistic simulations of wetting properties and water films on hydrophilic surfaces,” J. Chem. Phys. **146**, 164705 (2017).
- ³⁴M. Kanduč, “Going beyond the standard line tension: Size-dependent contact angles of water nanodroplets,” J. Chem. Phys. **147**, 174701 (2017).

- ³⁵D. Surbllys, F. Leroy, Y. Yamaguchi, and F. Müller-Plathe, “Molecular dynamics analysis of the influence of coulomb and van der waals interactions on the work of adhesion at the solid-liquid interface,” *J. Chem. Phys.* **148**, 134707 (2018).
- ³⁶C. Bistafa, D. Surbllys, H. Kusudo, and Y. Yamaguchi, “Water on hydroxylated silica surfaces: Work of adhesion, interfacial entropy, and droplet wetting,” *J. Chem. Phys.* **155**, 064703 (2021).
- ³⁷E. M. Grzelak and J. R. Errington, “Computation of interfacial properties via grand canonical transition matrix monte carlo simulation,” *J. Chem. Phys.* **128**, 014710 (2008).
- ³⁸G. V. Lau, I. J. Ford, P. A. Hunt, E. A. Müller, and G. Jackson, “Surface thermodynamics of planar, cylindrical, and spherical vapour-liquid interfaces of water,” *J. Chem. Phys.* **142**, 114701 (2015).
- ³⁹B. Kumar and J. R. Errington, “The use of monte carlo simulation to obtain the wetting properties of water,” *Physics Procedia* **53**, 44–49 (2014).
- ⁴⁰V. R. Ardham, G. Deichmann, N. F. van der Vegt, and F. Leroy, “Solid-liquid work of adhesion of coarse-grained models of n-hexane on graphene layers derived from the conditional reversible work method,” *J. Chem. Phys.* **143**, 243135 (2015).
- ⁴¹H. Jiang, F. Müller-Plathe, and A. Z. Panagiotopoulos, “Going beyond the standard line tension: Size-dependent contact angles of water nanodroplets,” *J. Chem. Phys.* **147**, 084708 (2017).
- ⁴²S. Ravipati, B. Aymard, S. Kalliadasis, and A. Galindo, “On the equilibrium contact angle of sessile liquid drops from molecular dynamics simulations,” *J. Chem. Phys.* **148**, 164704 (2018).
- ⁴³T. Omori, Y. Kobayashi, Y. Yamaguchi, and T. Kajishima, “Understanding the asymmetry between advancing and receding microscopic contact angles,” *Soft Matter* **15**, 3923–3928 (2019).
- ⁴⁴R. Bey, B. Coasne, and C. Picard, “Probing the concept of line tension down to the nanoscale,” *J Chem. Phys.* **152**, 094707 (2020).
- ⁴⁵A. Rode, S. Hyde, E. Gamaly, R. Elliman, D. McKenzie, and S. Bulcock, “Structural analysis of a carbon foam formed by high pulse-rate laser ablation,” *Appl. Phys. A Mater. Sci. Process.* **69**, S755–S758 (1999).
- ⁴⁶K. Falk, N. Fillot, A.-M. Sfarghiu, Y. Berthier, and C. Loison, “Interleaflet sliding in lipidic bilayers under shear flow: comparison of the gel and fluid phases using reversed

- non-equilibrium molecular dynamics simulations,” *Phys. Chem. Chem. Phys.* **16**, 2154–66 (2014).
- ⁴⁷Y. Homma, S. Chiashi, T. Yamamoto, K. Kono, D. Matsumoto, J. Shitaba, and S. Sato, “Photoluminescence measurements and molecular dynamics simulations of water adsorption on the hydrophobic surface of a carbon nanotube in water vapor,” *Phys. Rev. Lett.* **110**, 1–4 (2013).
- ⁴⁸K. Imadate and K. Hirahara, “Experimental determination of the diameter-dependent wettability of carbon nanotubes as studied using atomic force microscopy,” *Phys. Chem. Chem. Phys.* **20**, 26979–26985 (2018).
- ⁴⁹R. C. Tolman, “The Effect of Droplet Size on Surface Tension,” *J. Chem. Phys.* **17**, 333–337 (1949).
- ⁵⁰E. M. Blokhuis and J. Kuipers, “Thermodynamic expressions for the Tolman length,” *J. Chem. Phys.* **124**, 074701 (2006).
- ⁵¹S. Tumram, K. Kesava Rao, and M. S. Ananth, “Augmented Gibbs–Tolman Model for Surface Tension,” *Langmuir* **33**, 11687–11697 (2017).
- ⁵²J. A. W. Elliott, “Surface thermodynamics at the nanoscale,” *J. Chem. Phys.* **154**, 190901 (2021).
- ⁵³H. Yaguchi, T. Yano, and S. Fujikawa, “Molecular dynamics study of vapor-liquid equilibrium state of an argon nanodroplet and its vapor,” *J. Fluid. Sci. Tech.* **5**, 180 (2010).
- ⁵⁴S. K. Das and K. Binder, “Universal Critical Behavior of Curvature-Dependent Interfacial Tension,” *Phys. Rev. Lett.* **107**, 235702 (2011).
- ⁵⁵B. Cheng and M. Ceriotti, “Communication: Computing the Tolman length for solid-liquid interfaces,” *J. Chem. Phys.* **148**, 231102 (2018).
- ⁵⁶P. Rehner and J. Gross, “Surface tension of droplets and Tolman lengths of real substances and mixtures from density functional theory,” *J. Chem. Phys.* **148** (2018), 10.1063/1.5020421.
- ⁵⁷Y. Gao, K. Wu, Z. Chen, W. Tian, J. Li, Z. Huang, and J. Bi, “Model for Interfacial Tension of Nanoconfined Lennard-Jones Fluid,” *Energy & Fuels* **35**, 4044–4052 (2021).
- ⁵⁸P. Montero de Hijes, J. R. Espinosa, E. Sanz, and C. Vega, “Interfacial free energy of a liquid-solid interface: Its change with curvature,” *J. Chem. Phys.* **151**, 144501 (2019).
- ⁵⁹S. Plimpton, “Fast parallel algorithms for short-range molecular dynamics,” *J. Comp. Phys* **117**, 1–19 (1995).

- ⁶⁰“GROMACS 4: Algorithms for Highly Efficient, Load-Balanced, and Scalable Molecular Simulation.” *J. Chem. Theory Comput.* **4**, 435–447 (2008).
- ⁶¹S. M. Thompson, K. E. Gubbins, J. P. R. B. Walton, R. A. R. Chantry, and J. S. Rowlinson, “A molecular dynamics study of liquid drops,” *J. Chem. Phys.* **81**, 530–542 (1984).
- ⁶²E. A. Mastny and J. J. de Pablo, “Melting line of the Lennard-Jones system, infinite size, and full potential,” *J. Chem. Phys.* **127**, 104504 (2007).
- ⁶³H. Kusudo, T. Omori, and Y. Yamaguchi, “Local stress tensor calculation by the method-of-plane in microscopic systems with macroscopic flow: A formulation based on the velocity distribution function,” *J. Chem. Phys.* **155**, 184103 (2021).